

NAVAL POSTGRADUATE SCHOOL

Monterey, California



Detection and Parameter Estimation of Chirped Radar Signals

by

R. Hippenstiel
M. P. Fargues
I. Moraitakis
C. Williams

January 10, 2000

Approved for public release; distribution is unlimited.

Prepared for: Center for Reconnaissance Research
Naval Postgraduate School

DTIC QUALITY INSPECTED 4

20000203 029

NAVAL POSTGRADUATE SCHOOL
Monterey, California

RADM ROBERT C. CHAPLIN
Superintendent

R. Elster
Provost

This report was sponsored by the Naval Postgraduate School Center for Reconnaissance Research.

Approved for public release; distribution is unlimited.

The report was prepared by:

Ralph Hippensiel

RALPH HIPPENSTIEL
Associate Professor
Department of Electrical and
Computer Engineering



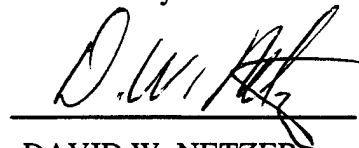
Monique P. Fargues
MONIQUE P. FARGUES
Associate Professor
Department of Electrical and
Computer Engineering

Reviewed by:



JEFFREY B. KNORR
Chairman
Department of Electrical and
Computer Engineering

Released by:



David W. Netzer
DAVID W. NETZER
Associate Provost and
Dean of Research

REPORT DOCUMENTATION PAGE			Form Approved OMB No. 0704-0188
<p>Public reporting burden for the collection of information is estimated to average 1 hour per response, including the time for reviewing instructions, searching existing data sources, gathering and maintaining the data needed, and completing and reviewing the collection of information. Send comments regarding this burden estimate or any other aspect of this collection of information, including suggestions for reducing this burden to Washington Headquarters Services, Directorate for Information Operations and Reports, 1215 Jefferson Davis Highway, Suite 1204, Arlington VA 22202-4302, and to the Office of Management and Budget: Paperwork Reduction Project (0704-0188), Washington DC 20503.</p>			
1. AGENCY USE ONLY (Leave blank)	2. REPORT DATE	3. REPORT TYPE AND DATES COVERED	
	January 10, 2000	Final Report, Sep 98-Dec 99	
4. TITLE AND SUBTITLE		5. FUNDING NUMBERS	
Detection and Parameter Estimation of Chirped Radar Signals		MIPR NO. 448-991831	
6. AUTHOR(S)			
R. Hippenstiel, M.P. Fargues, I. Moraitakis, and C. Williams			
7. PERFORMING ORGANIZATION NAME(S) AND ADDRESS(ES)		8. PERFORMING ORGANIZATION REPORT NUMBER	
Department of Electrical and Computer Engineering Naval Postgraduate School Monterey, CA 93943-5000		NPS-EC-00-001	
9. SPONSORING/MONITORING AGENCY NAME(S) AND ADDRESS(ES)		10. SPONSORING/MONITORING AGENCY REPORT NUMBER	
Center for Reconnaissance Research Naval Postgraduate School Monterey, CA 93943			
11. SUPPLEMENTARY NOTES The views expressed in this report are those of the author and do not reflect the official policy or position of the Department of Defense or the United States Government.			
12a. DISTRIBUTION/AVAILABILITY STATEMENT Approved for public release; distribution is unlimited.		12b. DISTRIBUTION CODE A	
13. ABSTRACT (Maximum 200 words) This work investigates the detection of pulses and extraction of modulation parameters from different types of time-limited chirp signals, as may be found in pulse-compression radar signals. The work is split into two parts. The first part investigates the pulse detection problem. Such information can be used to determine the pulse width and repetition rate of the radar systems under investigation in an automated fashion. We compare the robustness of three TFC-based schemes and an envelope detection algorithm in noisy environments. Results show that none of the pulse detection schemes considered in this work to be clearly better than the others for the SNR range considered, and the specific selection to be a function of the desirable characteristic, either P_{FA} or P_D , to be optimized. The second part of the work focuses on the extraction of linear and hyperbolic chirp modulation parameters. First, time-frequency/scale images of the extracted pulses are generated, next, additional processing applied to the images allow the identification of the modulation parameters. Eleven different types of time-frequency and wavelet-based transformations are considered and applied to chirp signals in additive white Gaussian noise. Results show time-frequency transformations to lead to better focused images when dealing with noisy signals, and thereby to better estimation of the modulation parameters than the wavelet-based decompositions do. Simulations investigate the robustness of the resulting modulation estimation schemes in noise environments.			
14. SUBJECT TERMS Radar processing, time-frequency/scale distributions, electrical warfare			15. NUMBER OF PAGES 93
			16. PRICE CODE
17. SECURITY CLASSIFICATION OF REPORT UNCLASSIFIED	18. SECURITY CLASSIFICATION OF THIS PAGE UNCLASSIFIED	19. SECURITY CLASSIFICATION OF ABSTRACT UNCLASSIFIED	20. LIMITATION OF ABSTRACT SAR

CONTENTS

LIST OF FIGURES.....	VI
EXECUTIVE SUMMARY	VII
I. INTRODUCTION.....	1
A. BACKGROUND.....	1
B. STUDY ORGANIZATION.....	1
II. MODERN RADAR.....	3
A. RF AGILITY.....	3
B. INTERPULSE MODULATION.....	4
1. PRF Switching	4
2. Staggered PRF.....	5
3. Sliding PRF.....	5
4. Jittered PRF	5
C. INTRA-PULSE MODULATION	6
1. Frequency Modulation on the Pulse (FMOP).....	7
2. Phase Modulation on the Pulse (PMOP).....	7
3. FMOP and PMOP Comparison.....	8
D. COMBINING TECHNIQUES.....	8
III. TEMPORAL CORRELATION FUNCTION.....	9
A. CORRELATION FUNCTION DEFINITION	9
B. INSTANTANEOUS CORRELATION FUNCTION DEFINITION	9
C. HILBERT TRANSFORM.....	11
D. MEDIAN FILTERING.....	11
IV. SIGNAL ANALYSIS TECHNIQUES AND SIMULATION.....	12
A. PULSE GENERATION	12
B. DETECTION TECHNIQUES	12
C. SIMULATION RESULTS.....	15
V. TIME-FREQUENCY REPRESENTATIONS.....	23
A. BACKGROUND.....	23
B. INTRODUCTION.....	23
C. TIME-FREQUENCY REPRESENTATIONS DESCRIPTION	25
1. <i>Introduction</i>	25
2. <i>Description</i>	27
VI. APPLICATION OF THE RADON TRANSFORM TO LINEAR CHIRP PARAMETERS ESTIMATION	33
A. INTRODUCTION.....	33

B.	LINE PARAMETER IDENTIFICATION	35
C.	LINEARLY MODULATED CHIRPS	37
1.	<i>Signal Generation</i>	38
2.	<i>Simulation Set-up and Extraction</i>	40
3.	<i>Performance Results</i>	44
3.a)	<i>Evaluation of Time-frequency Representations</i>	44
3.b)	<i>Error Evaluation</i>	53
3.c)	<i>Multi-pulse processing results</i>	55
3.d)	<i>Application to the AN/SPS-40B radar</i>	56
4.	<i>Comparisons</i>	59
4.a)	<i>Introduction</i>	59
4.b)	<i>Simulations</i>	61
VII.	HYPERBOLIC CHIRP PARAMETERS ESTIMATION.....	63
A.	SIGNAL GENERATION.....	63
1.	<i>Introduction</i>	63
2.	<i>Hyperbolic Line Parameter Constraints</i>	65
B.	FEATURE EXTRACTION.....	68
1.	<i>Introduction</i>	68
2.	<i>Method Description</i>	70
C.	SIMULATION RESULTS	74
VIII.	CONCLUSIONS.....	79
	REFERENCES	81
	Distribution List.....	85

LIST OF FIGURES

<i>Figure IV.1: Envelope-based and TCF-based detectors.</i>	<i>15</i>
<i>Figure IV.2: Performance curve; normalized percentage versus noise sigma; SNR=20dB.</i>	<i>17</i>
<i>Figure IV.3: Performance curve; normalized percentage versus noise sigma; SNR=10dB.</i>	<i>18</i>
<i>Figure IV.4: Performance curve; normalized percentage versus noise sigma; SNR=6dB.</i>	<i>19</i>
<i>Figure V.1: Various time-frequency representations, linear chirp, SNR=10dB, Frequency normalized to sampling frequency.</i>	<i>26</i>
<i>Figure V.2: Wigner-Ville distribution; time normalized to the pulse length.</i>	<i>28</i>
<i>Figure V.3: Pseudo Wigner-Ville distribution; time is normalized over the pulse duration.</i>	<i>29</i>
<i>Figure V.4: Smoothed Pseudo Wigner-Ville distribution; time is normalized over the pulse duration.</i>	<i>30</i>
<i>Figure V.5: Reassignment method applied to a hyperbolic chirp test signal; time is normalized over the pulse duration.</i>	<i>31</i>
<i>Figure VI.1: Two-dimensional Radon transform.</i>	<i>34</i>
<i>Figure VI.2: Radon transform geometry; image containing a single line.</i>	<i>36</i>
<i>Figure VI.3: Radon transform for line shown in Figure VI.2; for $\vartheta=0^\circ, \dots, 180^\circ$, 1° inc.</i>	<i>37</i>
<i>Figure VI.4: Synthetic radar signal; linear chirp modulation.</i>	<i>38</i>
<i>Figure VI.5: Various time-frequency representations for a linear chirp; SNR=10dB, Normalized frequency. Frequency normalized to sampling frequency.</i>	<i>43</i>
<i>Figure VI.6: Time-frequency image for a linear chirp; normalized frequency ($f_s = 1$), starting frequency $f_0 = .2$ and ending frequency $f_1 = 0.4$.</i>	<i>45</i>
<i>Figure VI.7: Slope and offset errors for wavelet and cosine packet, wavelet and cosine pursuit decompositions for linear chirp signals; SNR given in dB.</i>	<i>46</i>
<i>Figure VI.8: Slope and offset errors for the PWV, reassigned PWV, SPWV, and reassigned SPWV decompositions; linear chirp signals; SNR given in dB.</i>	<i>47</i>
<i>Figure VI.9: Slope and offset errors for the Wigner-Ville decomposition, Spectrogram, and reassigned Spectrogram; linear chirp signals; SNR given in dB.</i>	<i>48</i>
<i>Figure VI.10: Linear chirp trial case 1; SNR=-10dB; true and estimated modulation parameters.</i>	<i>50</i>
<i>Figure VI.11: Linear chirp trial case 2; SNR=-10dB; true and estimated modulation parameters.</i>	<i>51</i>
<i>Figure VI.12: Slope and offset error for the SPWV distribution; five realizations.</i>	<i>56</i>
<i>Figure VI.13: Instantaneous frequency for the heterodyned signal; Normalized frequency $f_s = 1$.</i>	<i>59</i>
<i>Figure VI.14: Slope and offset errors obtained with Peleg and Porat' scheme; linear chirp signals [25]; 100 trials per SNR level; left plot: slope error; right plot: offset error.</i>	<i>62</i>
<i>Figure VII.1: Hyperbolic modulation; normalized frequency for $a=10$, $n_0=25$, $b=0.05$.</i>	<i>65</i>
<i>Figure VII.2: Maximum distance between a hyperbolic line and its chord; $a=12$, $n_0=25$, $b=0$.</i>	<i>67</i>
<i>Figure VII.3: Extraction of the instantaneous normalized frequency expression from the time-frequency image. Before and after median smoothing, $L=5$.</i>	<i>69</i>
<i>Figure VII.4: Normalized errors obtained for a, b, n_0; 150 randomly generated hyperbolic chirps.</i>	<i>73</i>
<i>Figure VII.5: Two hyperbolic lines; Solid line: true hyperbolic curve ($a=65$, $b=0.1$ and $n_0=240$, dotted line: estimated hyperbolic curve ($a=84$, $b=0.08$ and $n_0=294$).</i>	<i>75</i>
<i>Figure VII.6: Hyperbolic chirp; normalized errors for the SPWV distribution.</i>	<i>76</i>
<i>Figure VII.7: Hyperbolic chirp; normalized errors for the RPWV distribution.</i>	<i>77</i>
<i>Figure VII.8: Hyperbolic chirp; normalized errors for the RSPWV distribution.</i>	<i>78</i>

EXECUTIVE SUMMARY

This work investigated the detection of pulses and extraction of modulation parameters from different types of time-limited chirp signals, as may be found in pulse-compression radar signals. The work is split into two parts. The first part examines the pulse detection problem, i.e., the detection of the pulse start/stop times. Such information can be used to determine the pulse width and repetition rate of the radar systems under investigation in an automated fashion. We compare the robustness of three TCF-based schemes and an envelope detection algorithm in noisy environments. Results show that none of the pulse detection schemes considered in this work to be clearly better than the others for the SNR range considered, and the specific selection to be a function of the desirable characteristic, either P_{FA} or P_D , to be optimized.

The second part of the work focuses on the extraction of modulation parameters from two specific modulation types: linear and hyperbolic chirp modulation. For the second part it is assumed that: 1) individual pulses have been detected and isolated prior to the processing, and 2) the modulation type is known, as we do not discuss issues related to the specific identification of the modulation scheme which are left for further research. The main idea behind the work reported in this section is the fact that we use an image processing approach. First, time-frequency/scale images of the extracted pulses are generated, next additional processing applied to the images allow the identification of the modulation parameters. Thus, different types of time-frequency and wavelet-based transformations are considered and applied to linear chirp signals in additive white

Gaussian noise. Results show that time-frequency transformations lead to better focused images when dealing with noisy signals, and thereby to better estimation of the modulation parameters than the wavelet-based decompositions do. Simulations investigate the robustness of the modulation estimation schemes in noisy environments both for linear and hyperbolic chirps.

I. INTRODUCTION

A. BACKGROUND

Numerous schemes have been proposed over the years to retrieve modulation parameters of chirp signals for various types of applications ranging from communications to radar and sonar. The capability to extract the modulation parameters in an automated fashion can be very useful as such procedures can be integrated in monitoring schemes. The report focuses on signals with constant amplitudes and various types of modulation types, such as constant, linear and hyperbolic intra-pulse frequency modulation over a given pulse. These modulation types can be found in pulse-compression radar signals, pulse or CW radar signals received from targets, or modulation signals found in communication applications. Radar intra-pulse modulation parameters are usually extracted using hardware schemes, as they are well suited to extract the instantaneous frequency at high SNR levels. This study considers the problem from a different angle and investigates the application of temporal correlation functions (TCF), time-frequency (TF) and time-scale (wavelet) transformations, and basic image processing techniques to detect pulse location and extract modulation information.

B. STUDY ORGANIZATION

This work was split into two parts. The first part examined the pulse detection problem, i.e., the detection of the pulse start/stop times, and compared several TCF-based detection schemes. This information can be used to determine the pulse width and

repetition rate of the radar systems under investigation. The second part of the work focused on the extraction of modulation parameters from two specific modulation types: linear and hyperbolic chirp modulation. For the second part it is assumed that: 1) individual pulses have been detected and isolated prior to the processing discussed next, and 2) the modulation type is known, as we do not discuss issues related to the specific identification of the modulation scheme which is left for further research.

Chapter II presents a brief review of RADAR concepts. Chapter III presents the concept of temporal correlation in the context of pulse detection. Chapter IV describes the various TCF-based signal analysis techniques considered and the detection performances obtained for pulses distorted by white Gaussian noise. Chapter V briefly describes the time-frequency transformations considered in this work to extract intra-pulse modulation parameters. The application of TF and Radon transforms to extract the modulation parameters from linear chirps is discussed in Chapter VI. Next, we considered the extraction of modulation parameters for hyperbolic chirps. We restricted our study to the top three energy TF transformations leading to the best image quality for the linear chirp, and derived the estimation procedure presented in Chapter VII. Finally, conclusions and recommendations for further research are presented in Chapter VIII.

II. MODERN RADAR

Radar signal identification and parameter identification would be simple if radars operated at a fixed frequency with constant parameters. Modern techniques have improved the radar's unambiguous detection range, range resolution, and the radar's susceptibility to jamming while lowering the power requirements. These modifications tend to make the radar recognition easier, but they tend to make the detection and extraction of the parameters more difficult.

The modifications tend to fall into three general categories: RF agility, inter-pulse and intra-pulse modulation. Some examples of the techniques and what improvements they can provide are discussed next.

A. RF AGILITY

Radiating frequency (RF) agility is the ability to change the operating frequency on a pulse to pulse basis. There are many advantages to using an RF agile radar, although the Electronic Counter Counter Measure (ECCM) capability is generally the most emphasized improvement.

Pulse frequency agile radars, particularly when the frequencies are randomized over the operating range of the radar, are difficult to jam [42]. RF agility is also used to reduce the angular error in the radar caused by glint. Glint is produced when echoes are treated as if they are coming from one scattering center, instead of an echo vector sum returned from the different scattering centers of an extended target. By using multiple frequencies, selecting the frequency with the strongest return tends to eliminate the large

angle errors. The minimum frequency difference between pulses required for glint reduction is given by

$$\Delta f = \frac{2}{2D}. \quad (\text{II.1})$$

Pulse to pulse frequency agility is a successful technique to counter ECCM. Radars can also employ a dwell and switch RF hopping scheme. In this case, a given frequency for a number of pulses or scans is used followed by a jump to another frequency. The frequencies are usually discretely spaced in a given band. The frequency hop can occur after a set number of pulses, after a set scan time, or with a PRF jump.

B. INTERPULSE MODULATION

Inter-pulse modulation refers to the modulation of the PRF or PRI of a radar pulse train. This combines the advantages of a low with that of a high PRF radar. These techniques also minimize range eclipsing which occurs when the target's echo arrives during the next pulse receive cycle. PRF modulation does not require complex circuits, so it is often used to improve the radar performance. Four common techniques are described below [41].

1. PRF Switching

A PRF switching radar switches between a few discrete PRF's. Typically one PRF will be used for a set time interval such as one scan interval or a given number of pulses, which is then switched to another PRF for the next period. Some RF agile radars can also hop in frequency as the PRF switch occurs.

Careful selection of the PRF's can extend the blind speeds beyond the range of expected values. Only two or three discrete PRF values are necessary to resolve most ambiguous range problems [41].

2. Staggered PRF

The PRF switches on a pulse to pulse basis. This technique is mainly used to eliminate blind speeds and blind ranges [41]. Second time around clutter echoes do not cancel since the clutter does not appear at the same range from pulse to pulse. It takes several looks to determine whether or not a target is in motion [42].

3. Sliding PRF

The PRF is continuously varied, typically starting at a low and increasing to a high PRF value. Then the PRF jumps back to the low value to begin sliding again. Though the low-to-high variations tend to be repeated, the PRF values are not always the same [41].

By continuously increasing the PRF the target echo can not catch up with the range, and range eclipsing will not occur. Because of this, Sliding PRF is often used in target tracking radar [41].

4. Jittered PRF

The start time of each successive pulse is varied (jittered) relative to where it should have started in a regular pulse train. Jitter is normally classified by the percent jitter, which is the maximum jitter time divided by the normal pulse interval, and by the

manner in which the jitter time varies. The jitter may vary randomly from pulse to pulse but the actual variations may be from a pre-determined discrete set. The variation may also follow a sinusoidal, a triangular, or some other prescribed pattern [41].

Jittering the PRF improves the radar's performance both with respect to blind speed and the unambiguous range. Some commonly used jitter time distributions can improve both parameters by a factor of two or more [41].

C. INTRA-PULSE MODULATION

Intra-pulse modulation in conjunction with pulse compression delivers the power of a long pulse (a better maximum range) while keeping the range resolution of a short pulse. There are two methods to obtain intra-pulse modulation, frequency modulation of the pulse (FMOP) and phase modulation of the pulse (PMOP) [41].

Pulse compressed radars have a greater effective range and range resolution. They also are less susceptible to jamming as the jammer's power is spread over a larger bandwidth. Pulse compression radars are more tolerant of other radars operating in the same frequency spectrum (mutual interference). They can operate in a given spectral band with another pulse-compressed radar if each of them has its own characteristic modulation [42].

Some disadvantages of intra-pulse modulation are the increase in cost and complexity of the system. Also, the time sidelobes arising from compression can mask or be mistaken for a target [41].

Relative to short pulse radars, pulse compressed radars have the disadvantage of a longer minimum range. If the sidelobes are limited small signals may be lost. Finally, pulse compressed radars do not have the short pulse radars natural immunity to repeat jammers and range gate stealing jammers [42].

1. Frequency Modulation on the Pulse (FMOP)

A common type of FMOP uses linear frequency modulation. This modulation, also known as a “chirp”, linearly increases (or decreases) the frequency of the pulse over a small frequency range while holding the amplitude and pulse width constant. The receiver is designed so that all the frequencies arrive at the detector at the same time. This compresses the pulse to a bandwidth equal to the frequency shift of the pulse [41].

Another prominent FMOP technique is FM Stepping. The pulse is broken up into sub pulses that are held at a constant frequency, but stepped up or down by a discrete frequency value. The bandwidth of the compressed signal is the number of steps times the change in frequency [41].

2. Phase Modulation on the Pulse (PMOP)

The pulse is broken into N equal length sub pulses. Each of these sub pulses is either in phase or 180 degrees out of phase. The phase of the sub pulses is determined by a preset code, usually a Barker code or a pseudo random noise sequence. A matched filter cross correlates the received signal with a template. When the received signal and the template match up, the receiver returns a large peak [41].

3. FMOP and PMOP Comparison

The PMOP radar has a poor resolution in a dense target environment. PMOP radars benefit from the different phase coded sequences that can be assigned to different radars, so that a number of PMOP radars can operate in the same frequency band. PMOP radars are less susceptible to repeat jammers than FMOP radars are, since the code can be changed to counter a repeater mimicking it. FMOP radars are likely to be used when a wide bandwidth or very narrow compressed pulse is desired. A PMOP radar is likely to be used when jamming is a problem or when there will be multiple radars using the same portion of the frequency band [42].

D. COMBINING TECHNIQUES

While each of the three techniques have been discussed separately it is not unusual for a radar system to use a combination of these techniques. It is also important to note that a radar system may have multiple operational modes which can use any one or a combination of the techniques.

A typical example is a missile system radar. It may use a constant PRF while in a search mode, switch to an RF dwell and switch mode to acquire the target, and then switch to an RF agile, PRF staggered, chirped pulse modulation to track a target before launching a missile.

III. TEMPORAL CORRELATION FUNCTION

The temporal correlation function allows for non-stationary situations. It is indexed in time and in delay.

A. CORRELATION FUNCTION DEFINITION

Depending on the underlying process, various definitions are given to the auto-correlation function (ACF). The process may be deterministic, stochastic, finite-energy, infinite-energy, non-time-varying (stationary) or time-varying (non-stationary).

The ACF of a stochastic process is the correlation between two samples of the process taken at t_1 and t_2 , and is defined as:

$$R_{XX}(t_1, t_2) = E\{x(t_1)x^*(t_2)\}, \quad (\text{III.1})$$

where $E(\cdot)$ is the expectation operator and $*$ stands for the complex conjugation. For a stationary (or wide-sense stationary) process, $R(t_1, t_2)$ depends only on the time lag $\tau = t_1 - t_2$, resulting in a stationary spectrum. The Wiener-Khinchin theorem defines the relationship between the correlation function and spectral density as

$$S_{xx}(\omega) = \int R_{XX}(\tau) e^{-j\omega\tau} d\tau. \quad (\text{III.2})$$

B. INSTANTANEOUS CORRELATION FUNCTION DEFINITION

The ACF of deterministic and stochastic processes are computed using time domain averaging and the expectation operator, respectively. This means that a smoothing process has to be applied to compute the correlation functions. The

instantaneous correlation function (ICF) does not use an averaging operation (integration nor expectation). The instantaneous correlation function is defined as the product of two samples of the process. These two samples are drawn at two time instants centered about

time t . The instantaneous correlation function $R^i(t, \tau)$ is defined as:

$$R^i(t, \tau) = x(t + \frac{\tau}{2})x^*(t - \frac{\tau}{2}), \quad (\text{III.3})$$

where i denotes the instantaneous nature of the correlation function.

If $x(t)$ is a sinusoidal signal then the multiplication to obtain the instantaneous values of $R^i(t, \tau)$ generates cross terms in the ICF. For example, the real-valued sinusoidal signal $x(t) = A \cos(\omega t)$ has an ACF given by:

$$R(\tau) = \frac{A^2}{2} \cos(\omega\tau),$$

while the ICF is given by:

$$R^i(t, \tau) = \frac{A^2}{2} [\cos(2\omega\tau) + \cos(\omega\tau)].$$

The ACF of a single sinusoidal signal has only one component and no cross term, while the ICF has cross terms. If the signal $x(t)$ is represented by its analytic form $x(t) = Ae^{j\omega t}$, then its ICF is given by:

$$R^i(t, \tau) = A^2 e^{j\omega\tau}.$$

That is, the ICF of a single complex exponential signal has no cross-terms.

C. HILBERT TRANSFORM

The Hilbert transform allows the use of the analytic signal. In general taking the real valued signal and adding the Hilbert transform as the imaginary part accomplishes the analytic signal generation, i.e., one-sided spectral density. We note that in MATLAB taking the Hilbert transform amounts to generating the analytic signal.

D. MEDIAN FILTERING

Median filtering is a non-linear filtering technique that ranks the data in amplitude over a window of consideration and replaces the center of the window with the center (median) of the ranked data vector.

IV. SIGNAL ANALYSIS TECHNIQUES AND SIMULATION

A. PULSE GENERATION

For simulation purposes a frequency hopped radar pulse sequence (i.e., interpulse modulation) is generated, consisting of ten pulses. At each signal to noise (SNR) level 100 realizations are obtained, making a set of 1000 pulses available at each SNR level. The spacing between the ten pulses is randomized. The pulses can take on, in a random fashion, one of six possible carrier frequencies. The signals are used to obtain information about the false alarm rate (P_{FA}), the probability of detection (P_D), and what we define as the probability of multiple detection (P_{MUL}). The definition of P_{FA} and P_D are the classical ones, relating to the probability of detecting a pulse when there is noise only and the probability of detecting the pulse in the presence of noise, respectively. P_{MUL} denotes the improper detection of more than one pulse when only one pulse is present. This can be a problem in an automated detection system operating at low SNR levels or at high SNR levels if the threshold is set high. The experimental SNR ranges from 3 to 20 dB. For perfect detection and for perfect false alarm rate experiments SNR values from 6 to 20 dB are used.

B. DETECTION TECHNIQUES

Figure IV.1 shows the four processing techniques described in this chapter. The test signals are real valued, but when appropriate their analytic signal versions are processed [48]. Time domain data in real or analytic form is used to obtain the time

correlation function (TCF) or it is used directly in an envelope detector. The triangular sections of the TCF, indicating the time ranges when pulses are present, have noise and modulated signal components, while the remainder of the surface has noise only. In the description of the operation, i.e., Figure IV.1, the block labeled “Hilbert” denotes the operation to obtain the analytic signal. A detailed discussion of the TCF can be found in [46,47].

1. Real Processing:

Real valued data is used in the computation of the TCF. To extract the envelope of the TCF the absolute value of its analytic signal representation (denoted by Hilbert and the summation symbol) is taken. Next, the values are summed over both the $+45^\circ$ and -45° degree directions. The next processing step is a median filtering operation that smoothes the data but retains the sharp edges indicating the onset and the end of a pulse. The final procedure, used as the final step in all four processing techniques, is a threshold operation. The onset of a pulse and end of a pulse are declared when the threshold is crossed in an upward or downward fashion, respectively.

2. Triangle Processing:

This operation is identical to that described for the Real Processing technique with one exception. The exception is that the Hilbert transform, necessary for

obtaining an analytic signal is taken along the 45° angle, rather than the pre-programmed 90° directions.

3. Complex Processing :

For this processing technique the analytic signal representation of the time domain data is used. From the analytic (complex valued) data the TCF is computed. This operation is followed by sequentially taking the magnitude (absolute value) and the sum as described in the Real Processing technique, i.e., summing up the magnitudes in both the plus 45° and minus 45° degree directions. The next step is the median filtering operation to smooth the data. The final operation is the threshold operation. When the threshold is exceeded the onset of a pulse is declared. Conversely, the end of a given pulse is declared when falling below the threshold level.

4. Envelope Processing :

As the name implies the envelope is extracted by taking the absolute value of the analytic data (absolute value of the analytic signal values). The envelope of the data is filtered by a median filter, which is followed by the threshold detection mentioned before.

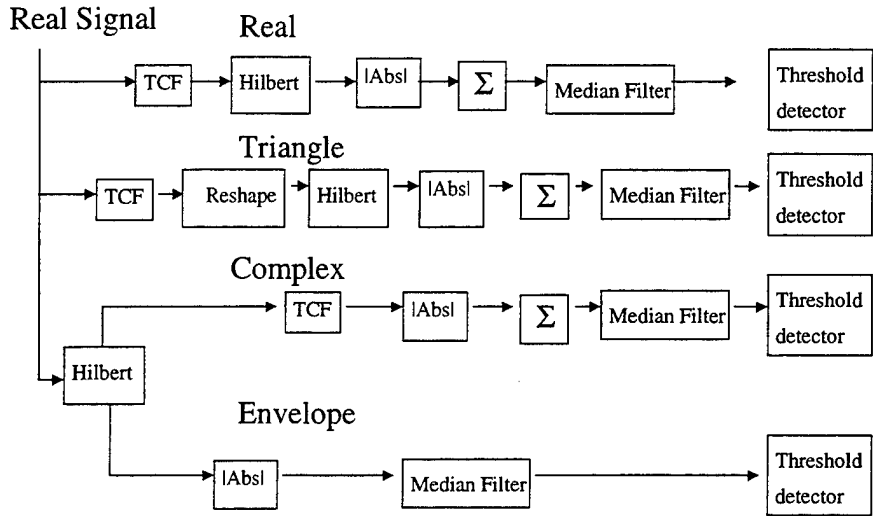


Figure IV.1: Envelope-based and TCF-based detectors.

Figure IV.1 shows the four processing techniques, outlined before, in a block diagram form. The top channel shows the “Real Processing” scheme, while the second channel shows the “Triangle Processing” technique. The third and fourth channel show the Complex and Envelope Processing techniques, respectively used.

C. SIMULATION RESULTS

Threshold sensitivity can be established by examining the number of pulses detected and the threshold. The threshold is expressed in integer multiples of the noise only standard deviation. Figures IV.2 to IV.4 show results for SNR values of 20dB, 10dB, and 6dB. In each graph the minimum threshold, in integer multiples of the noise only

standard deviation, which allows a false alarm rate of zero is provided. Each figure consists of four graphs, where each graph shows simulation results for one detector. There are four detection schemes, hence there are four graphs per figure. The SNR is fixed at a given value for the four graphs of a given figure.

Each graph can be broken into four sections. In the first section the threshold is too low, hence the noise causes false alarms. If the threshold is increased above the noise peaks only the signal is detected. If the threshold is further increased a region where the processed pulses begin to break apart, is reached. This causes the number of detected pulses to increase (a given pulse becomes multiple events, or multiple pulses). In the fourth region the number of detection begins to drop, eventually going to zero as the threshold is increased.

Each graph displays two curves. The lower one shows the probability of detection, while the upper one shows the total number of detection, expressed in a normalized percentage. For example, a value of 2.2 for the top trace, at a value of 0.9 for the lower trace, corresponds to a total number of detection of 220 percent with a probability of detection of 90% and a number of (improper) multiple detection of 130%. So for 1000 realizations, one has 900 proper detections, 1300 improper multiple detections and hence a total of 2,200 detections. This information is useful in assessing an appropriate threshold setting and to determine over what range of thresholds one can accurately detect the number of radar pulses.

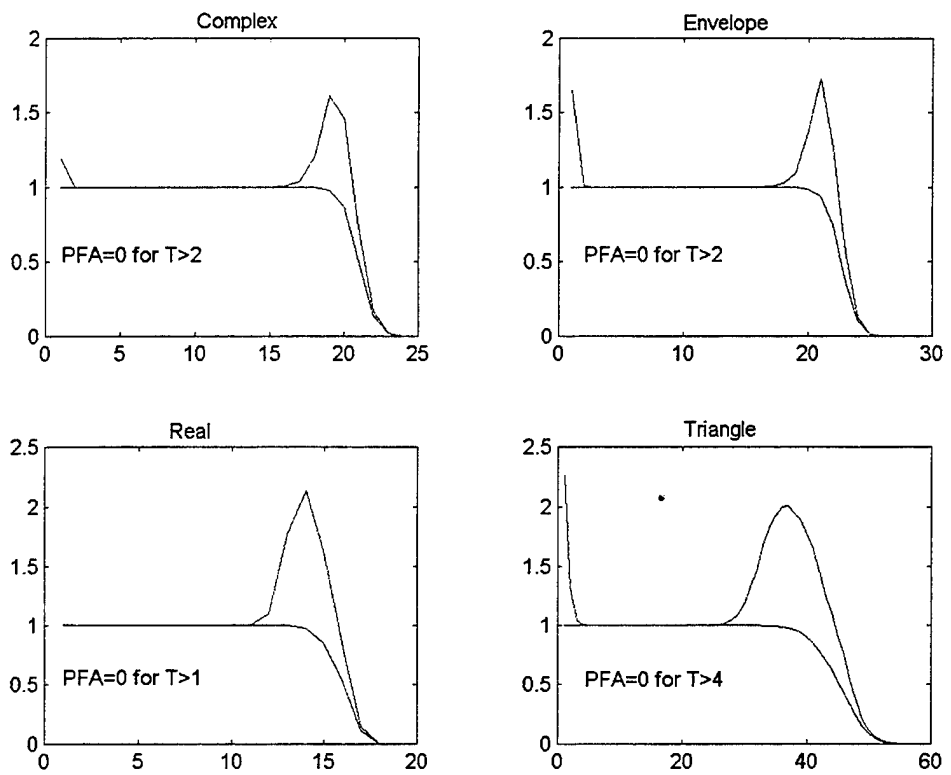


Figure 2a. Performance curve normalized percentage versus noise sigma, SNR=20dB.

Figure IV.2: Performance curve; normalized percentage versus noise sigma; SNR=20dB.

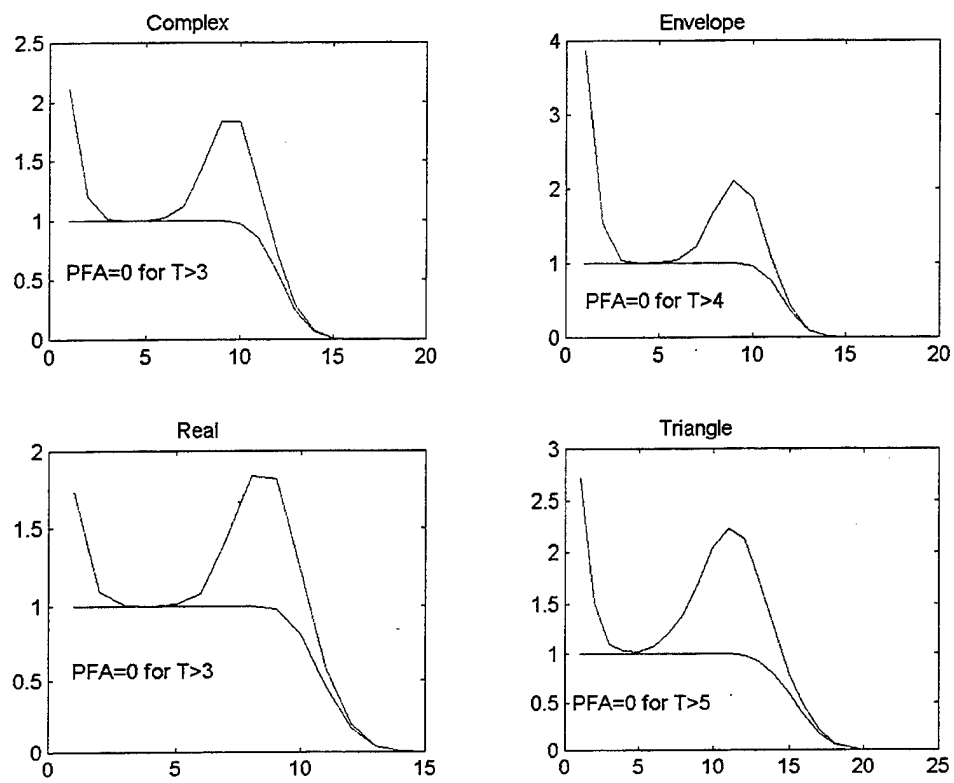


Figure 2b. Performance curve normalized percentage versus noise sigma, SNR=10dB.

Figure IV.3: Performance curve; normalized percentage versus noise sigma; SNR=10dB.

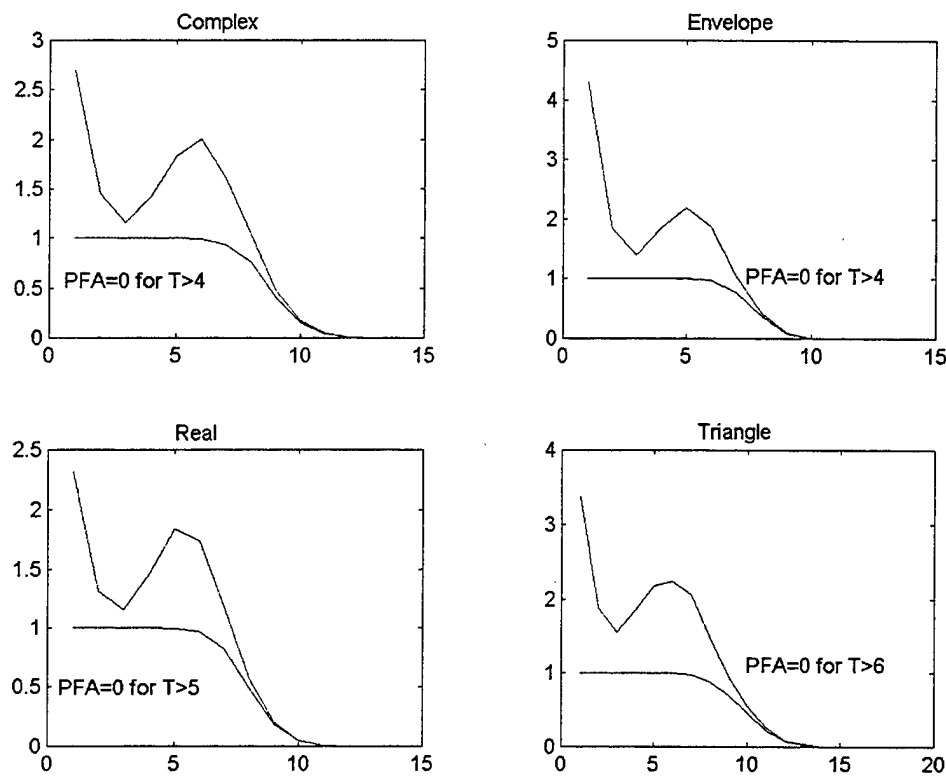


Figure 2c. Performance curve normalized percentage versus noise sigma, SNR=6dB.

Figure IV.4: Performance curve; normalized percentage versus noise sigma; SNR=6dB.

Table IV.1 uses a threshold of three noise standard deviations for each of the four detectors. It shows the performance in terms of the P_{FA} as a function of SNR for a P_D of 1.0, except when specially denoted. It is apparent that the Real (followed by the Complex) Processing scheme is the most promising one in the SNR range between 6 and 20 dB.

$P_D = 1.0$	20 dB	16 dB	13 dB	10 dB	6 dB	3 dB
TRIANGLE	0.046	0.056	0.060	0.095	0.165	0.236
COMPLEX	0	0	0.001	0.012	0.047	0.120
REAL	0	0	0	0.004	0.039	0.091 @ $P_{FA}=0.99$ 5
ENVELOPE	0	0.006	0.022	0.045	0.094	0.133 @ $P_{FA}=0.99$ 8

Table IV.1: Performance for fixed threshold.

Table IV.2 shows the performance in terms of the P_D as a function of SNR for a P_{FA} equal to 0. It is apparent that the Complex (followed by the Envelope) Processing scheme is the most promising one in the SNR range between 3 to 20 dB.

$P_{FA} =$ 0.0	20 dB	16 dB	13 dB	10 dB	6 dB	3 dB	0 dB
SNR							
TRIANGLE	1.0	1.0	1.0	1.0	0.973	0.438	0.036
COMPLEX	1.0	1.0	1.0	1.0	1.0	0.653	0.029
REAL	1.0	1.0	1.0	1.0	0.9677	0.479	0.071
ENVELOPE	1.0	1.0	1.0	1.0	1.0	0.312	0.017

Table IV.2: Performance for fixed $P_{FA} = 0$.

Table IV.3 allows the comparison of the detectors in terms of the sensitivity to the multiple detection of a given pulse. For the tests executed for this section, 100 realizations of a pulse train with 10 members is undertaken. This fixes the total number of possible pulses to 1000 for each SNR. The top line shows the number of properly detected pulses, while the lower line shows the number of multiple detection of the pulse trains. It is apparent that the Real, followed by the Envelope, detectors provide the most robust schemes.

$P_D = 1.0$	20 dB	16 dB	13 dB	10 dB	6 dB
SNR	20 dB	16 dB	13 dB	10 dB	6 dB
TRIANGLE	1000 0	1000 0	1000 0	1000 95	
COMPLEX	1000 0	1000 0	1000 0	1000 1694	
REAL	1000 0	1000 0	1000 0	1000 0	1000 1311
ENVELOPE	1000 0	1000 0	1000 0	1000 3	

Table IV.3: Detection versus SNR level.

It becomes apparent that with pulsed signals, depending on the importance of the undesirable characteristics, any of the three detectors (Complex, Real or Envelope) can be used. From the point of view of processing cost, the Envelope detector is preferable over the other two. From the point of false alarm rate or probability of detection the Complex or Real detector, respectively is more desirable.

V. TIME-FREQUENCY REPRESENTATIONS

A. BACKGROUND

Numerous schemes have been proposed over the years to retrieve modulation parameters of chirp signals for various types of applications ranging from communications to radar and sonar. This chapter focuses on signals with constant amplitudes and linear and hyperbolic intra-pulse modulation. Such types can be found in pulse-compression radar signals, pulse or CW radar signals received from targets, or modulation signals found in communication applications. Radar intra-pulse modulation parameters are usually extracted using hardware schemes, as they are well suited to extract the instantaneous frequency at high SNR levels. In this work we consider the problem from a different angle and investigate the application of time-frequency (TF) and basic image processing techniques to extract the modulation information.

This work assumes that 1) individual pulses have been detected and isolated prior to the processing discussed next, and 2) the modulation type is known, as we do not discuss issues related to the specific identification of the modulation scheme which is left for further research.

B. INTRODUCTION

Several different types of approaches to estimate the modulation parameters from chirp signals have been proposed in the literature over the years [25-31,33,34,36-40]. Maximum likelihood estimates of the chirp parameters can be derived in theory.

However they often lead to complicated algorithms, which may require n-dimensional optimization steps depending on the specific modulation type. Phase unwrapping techniques, application of the high-order ambiguity function [27], sub-optimal schemes to the maximum likelihood estimates [25], and others have also been proposed, each with its own advantages and drawbacks. In addition, combinations of TF representations and pattern recognition schemes have been considered to estimate chirp parameters [28-30,33,36].

Our study considers the combination of TF representations and pattern recognition schemes to estimate the chirp modulation parameters, and compare the resulting performances in various white Gaussian noise levels. The schemes proposed by Barbarossa et al. [28,29] and Wood and Barry [36] both combine the TFR-based Wigner-Ville (WV) transformation and the Radon (Hough) transform to estimate the chirp parameters, as the WV transform is well localized for linear chirps. Barbarossa also indicated that any TFR could potentially be considered, provided that it has good localization and concentration properties, and is robust to noise degradations. However, no performance comparisons were made available.

Our study considers a wide range of TFRs and identifies the top three representations best suited to the follow-on extraction scheme. We selected eleven different time-frequency and wavelet transformations (TFR) and applied a Radon-based transform step to extract the parameters from linear chirps, as discussed in Sections VI.B and VI.C. The selection of the top transformations was made by comparing the resulting errors in the estimation of the modulation parameters, as discussed in Section VI.C.3.

The second phase of the study considered the extraction of modulation parameters for hyperbolic chirps. We restricted our study to the top three energy distributions leading to the best image quality for the linear chirp, and derived the estimation procedure presented in Section VII.

C. TIME-FREQUENCY REPRESENTATIONS DESCRIPTION

1. Introduction

Generally, a signal can be represented using different types of decompositions. The two most widely used representations are the time domain and the frequency domain representation. The first shows how the amplitude of the signal changes with respect to time while the second shows how often these changes occur. However, the Fourier transform is not well suited to represent non-stationary signals, as it provides no exact information regarding the variations of the signal characteristics as a function of time. Analyzing such signals requires a joint time-frequency representation. Several techniques have been developed for this type of representation. This study considered the following eleven transformations from the two major classes of atomic decompositions and energy distributions. The goal was to select a small number of transformations leading to the best “image quality” from that set. We briefly introduce each of them. Further details regarding each of them may be found in Moraitakis [33, Sect. III]. The transformations considered are:

- Wavelet packet best basis,
- Cosine packet best basis,
- Wavelet pursuit,

- Cosine pursuit,
- Wigner-Ville distribution,
- Pseudo Wigner-Ville distribution,
- Reassigned Pseudo Wigner-Ville distribution,
- Smoothed Pseudo Wigner-Ville distribution,
- Reassigned Smoothed Pseudo Wigner-Ville distribution,
- Spectrogram distribution,
- Reassigned spectrogram distribution.

For comparison purposes, Figure V.1 shows the resulting images obtained for a linear chirp with SNR=10dB when no energy thresholding is applied to the images.

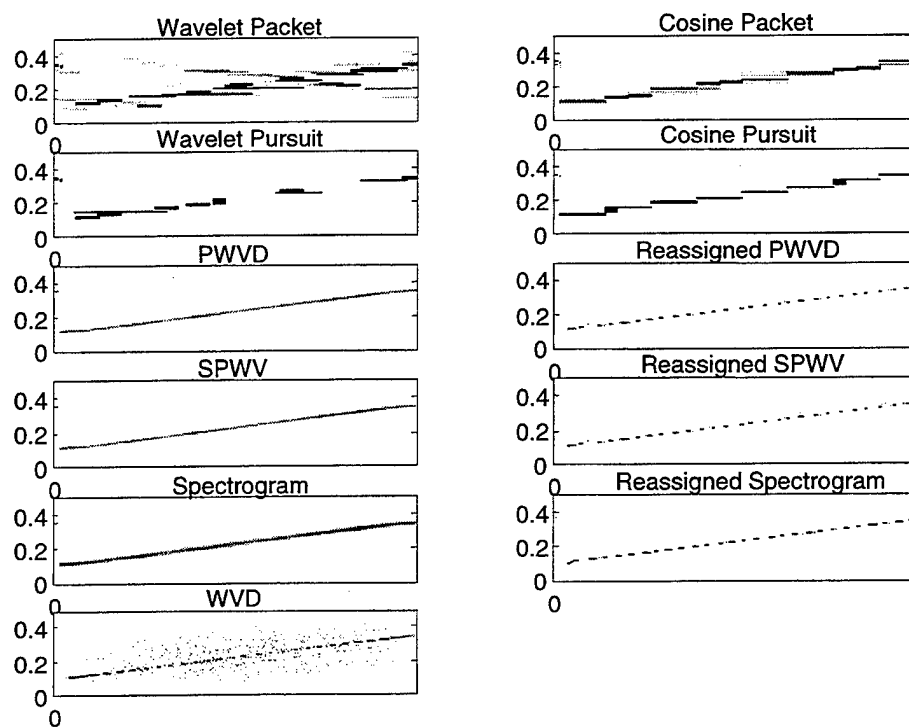


Figure V.1: Various time-frequency representations, linear chirp, SNR=10dB, Frequency normalized to sampling frequency.

2. Description

Wavelet and cosine decompositions were implemented with the software “Wavelab 7.01” software [12], while all others used the “Time-Frequency Toolbox” [9,11].

1. Wavelet packet best-basis decomposition (WPD):

This decomposition performs a multi-resolution decomposition by partitioning the frequency axis. It can be viewed as an extension of the wavelet transform where both high-pass and low-pass components are decomposed, thereby allowing for more flexibility in the decomposition than the wavelet transform does. Selection of the specific basis (called the “Best Basis”) is obtained by using a user-specified information cost criterion [3,5-7].

2. Cosine packet best-basis decomposition (CPD):

This decomposition is similar in concept to the WP decomposition, but performs a multi-resolution decomposition by partitioning the time axis instead. It is well matched to narrowband signals [5].

3. Wavelet pursuit (WP):

The wavelet pursuit is an iterative procedure where the signal is decomposed adaptively into a set of functions, not necessarily orthonormal. This procedure has been shown to be well suited to represent non-stationary signals with varying time-frequency characteristics [4,8].

4. Cosine pursuit (CP):

The cosine pursuit is similar in concept to the wavelet pursuit, where the signal is decomposed into a set of locally defined cosine functions [4].

5. Wigner-Ville distribution (WVD):

The WVD belongs to the Cohen's class of energy distributions [2,10]. It allows for perfect localization of linear chirps. However, its quadratic definition is responsible for interference terms that appear when the signal is not linearly modulated or more than one signal is present. Figure V.2 shows the WVD and the effect of the cross terms on four different signals. The effect is negligible in the noise-free linear chirp scenario only. Cross-terms show as a line between the two true components when the signal is composed of two parallel chirps.

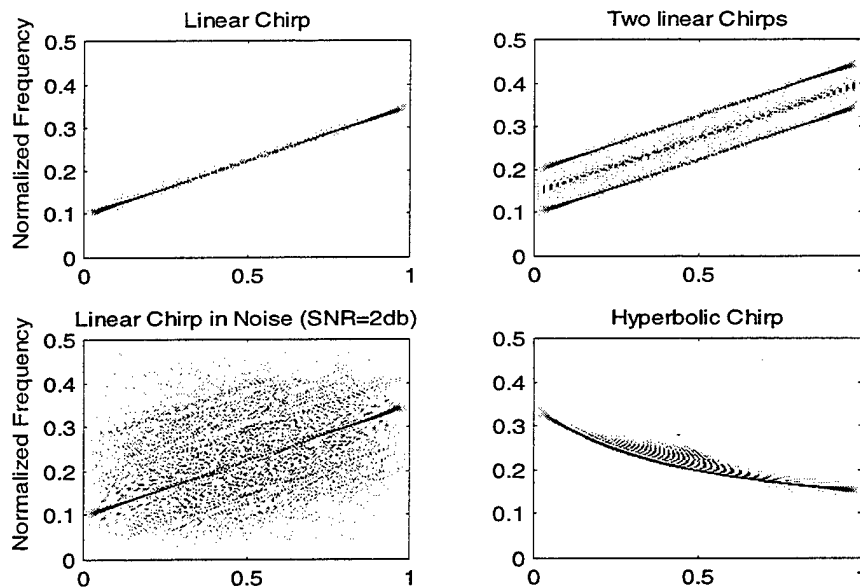


Figure V.2: Wigner-Ville distribution; time normalized to the pulse length.

6. Pseudo Wigner-Ville distribution (PWVD):

The PWVD introduces a time-window to the WVD definition, thereby reducing the interferences present in the transform, as illustrated in Figure V.3. However, the time windowing worsens the frequency resolution and the PWVD loses many of the valuable properties of the WVD [2].

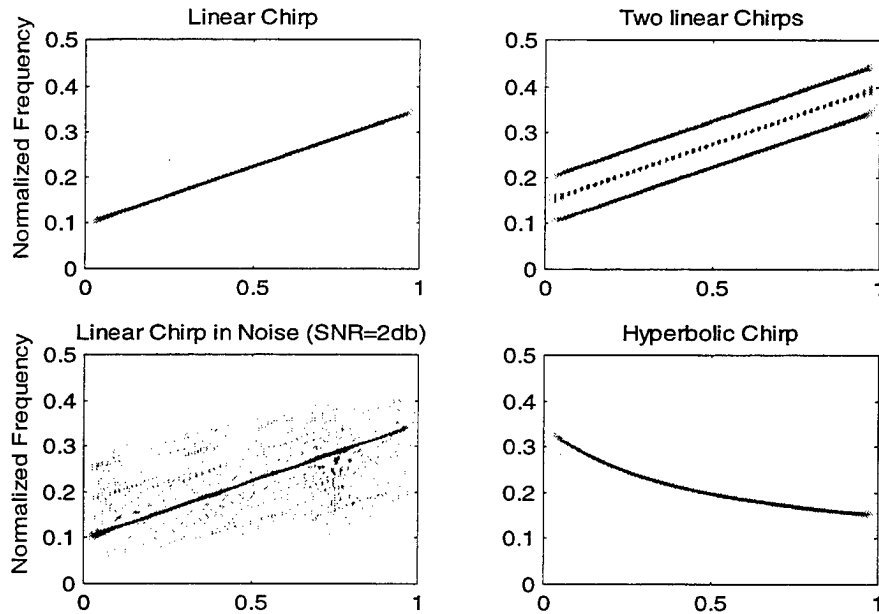


Figure V.3: Pseudo Wigner-Ville distribution; time is normalized over the pulse duration.

7. Smoothed Pseudo Wigner-Ville distribution (SPWVD):

The SPWD provides an attenuation of the interference terms by smoothing both in frequency and time domains. The drawback of this method is that the frequency resolution further degrades. Figure V.4 shows that the cross-terms have almost been eliminated while the frequency resolution has degraded.

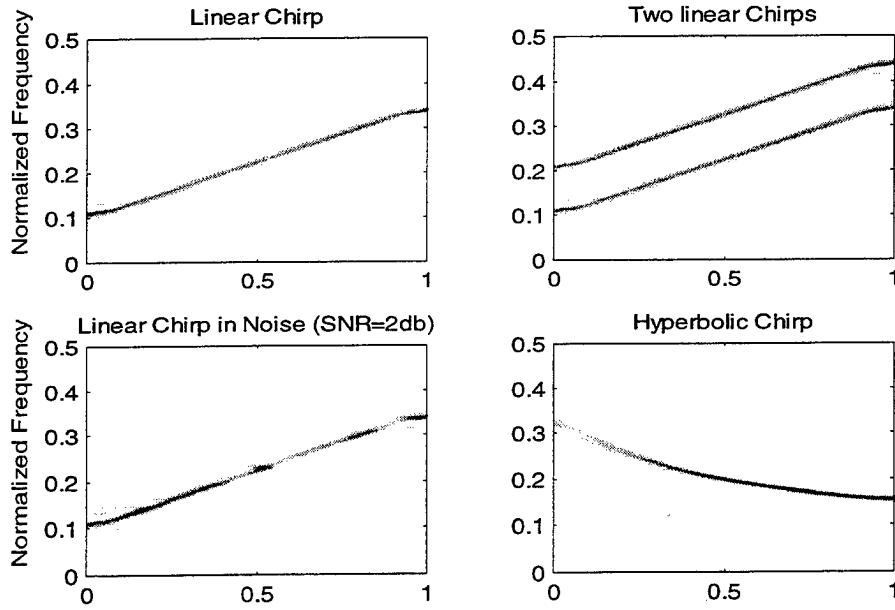


Figure V.4: Smoothed Pseudo Wigner-Ville distribution; time is normalized over the pulse duration.

8. Spectrogram:

The spectrogram is defined as the magnitude of the Short-Time Fourier transform

[2].

9. Reassigned spectrogram:

We see that the WVD resolution worsens when we try to suppress the interference terms. The reassignment method was introduced in an attempt to improve the resolution of the transformation [9]. This scheme assumes that the energy distribution in the time-frequency plane resembles a mass distribution and moves each value of the time-frequency plane located at a point (t, f) to another point (t', f') , which is the center of gravity of the energy distribution in the area of (t, f) . The result is a very focused

representation with high intensity since the value at the point (t', f') is the sum of all the neighboring values. The reassignment method can be applied to most energy distributions as well as to the spectrogram. However, the computational load is quite high. The top plot in Figure V.5 shows the hyperbolic chirp used in Figures V.2 to V.4, as represented for the reassigned spectrogram distribution.

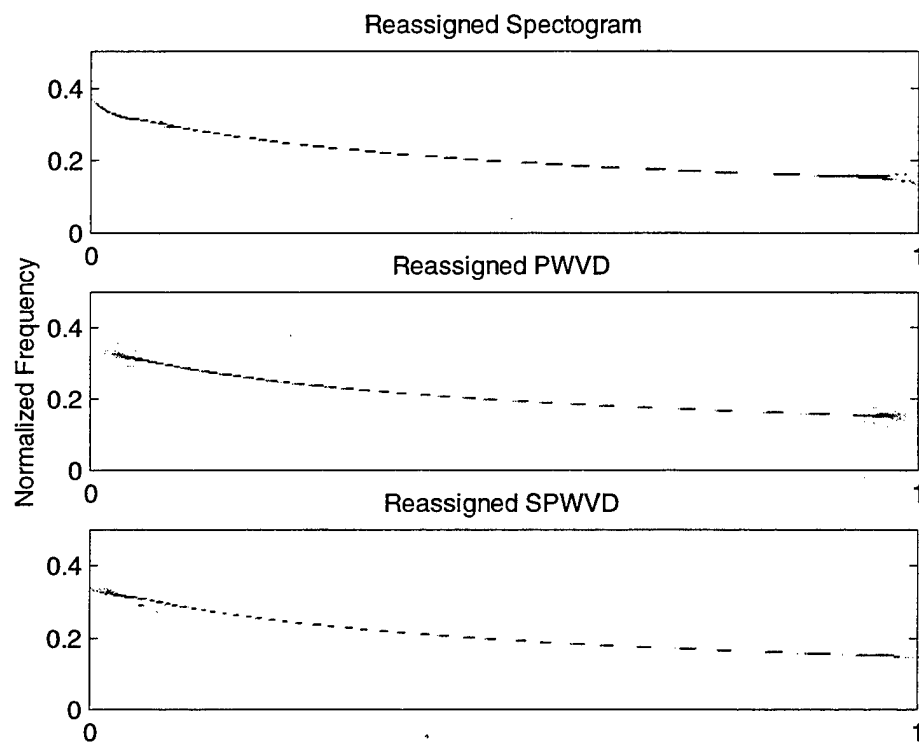


Figure V.5: Reassignment method applied to a hyperbolic chirp test signal; time is normalized over the pulse duration.

10. Reassigned Pseudo Wigner-Ville distribution (RPWVD):

The reassignment method, as discussed above, is applied to the PWVD. The middle plot in Figure V.2 shows the hyperbolic chirp used in Figures V.2 to V.4, as represented for the reassigned RPWVD.

11. Reassigned Smoothed Pseudo Wigner-Ville distribution (RSPWV):

The reassignment method, as discussed above, is applied to the SPWVD. The bottom plot in Figure V.5 shows the hyperbolic chirp used in Figures V.2 to V.4, as represented for the reassigned RSPWVD. Note the quality of the focusing in all three reassigned methods and the resulting lack of cross terms.

Simulations showed that the best image quality for the various time-frequency and time-scale representations of the noisy chirps is obtained with the time-frequency transformations, as illustrated in Figure V.1 above which shows a more focused representation of the information. Therefore, one would expect better estimation of the chirp parameters when using time-frequency representations than with time-scale representations as the SNR decreases. Section VI confirms these findings by investigating the estimation performance obtained from each of the time-frequency/scale transformations.

VI. APPLICATION OF THE RADON TRANSFORM TO LINEAR CHIRP PARAMETERS ESTIMATION

Once the time-frequency representation of the signal information is obtained, the Radon transform is applied to extract the modulation parameters for linear chirp signals. The Radon transform has been used extensively in image processing for edge detection [13,14] and has been generalized to detect curves of arbitrary shapes [17]. We briefly review its concept, before presenting its application to our problem.

A. INTRODUCTION

Let's assume we have an arbitrary function $f(x,y)$ in a subspace of \mathbb{R}^2 . The two-dimensional Radon transform is defined as the projection or line integral of the function $f(x,y)$ along all possible lines L [13]. Mathematically, the transformation is described as:

$$R = \int_L f(x(s,L), y(s,L))ds . \quad (\text{VI-1})$$

Recall that the equation of a line in polar coordinates is given by:

$$\rho = x \cdot \cos(\vartheta) + y \cdot \sin(\vartheta) , \quad (\text{VI-2})$$

where ρ and ϑ represent the distance from the origin and the angle measured counterclockwise from the x axis respectively, as shown in Figure VI.1. Now suppose we use another coordinate system with axes rotated by the angle ϑ . The new x -axis lies on the line with associated orthogonal direction "s". The two cartesian systems xoy and $\rho\vartheta s$ are related to each other via the following relation:

$$\begin{bmatrix} \rho \\ s \end{bmatrix} = \begin{bmatrix} \cos \vartheta & \sin \vartheta \\ -\sin \vartheta & \cos \vartheta \end{bmatrix} \cdot \begin{bmatrix} x \\ y \end{bmatrix}. \quad (\text{VI-3})$$

Equation (IV-1) can be rewritten as:

$$R(\rho, \vartheta) = \int_{-\infty}^{+\infty} f(\rho \cos \vartheta - s \sin \vartheta, \rho \sin \vartheta + s \cos \vartheta) \cdot ds \quad (\text{VI-4})$$

The above equation shows that the Radon transform translates a two-dimensional function of the variables (x, y) to one with variables (ρ, ϑ) . Thus, the Radon transform of an image taken at a specific angle ϑ is the projection of the image onto the line which forms an angle ϑ with the x -axis.

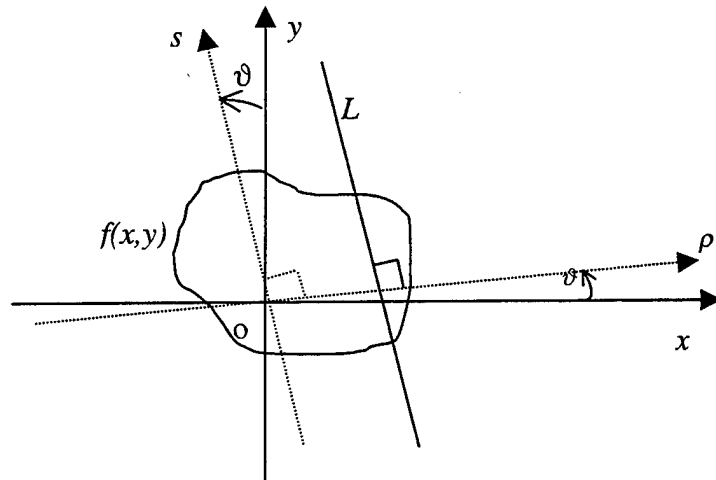


Figure VI.1: Two-dimensional Radon transform.

The Radon transform of a single line with a slope angle φ for the specific angle $\vartheta = \frac{\pi}{2} + \varphi$ is a single point with intensity equal to the sum of the intensities at each point

on the line. This property allows detection of lines in an image. In addition, the transform is also robust to noise degradations.

B. LINE PARAMETER IDENTIFICATION

Line parameters can be obtained using the Radon transform as follows: Assume the image under investigation contains a line which has an angle φ with the x-axis, as shown in Figure VI.2. The equation of the line can be defined in terms of its slope a and initial offset value b .

$$y = a \cdot x + b, \quad a = \tan(\varphi). \quad (\text{VI-5})$$

The Radon transform $R(\rho, \vartheta)$ of the image for angles 0° to 180° is maximum when the projection of the line has a minimum area. Thus, it is maximum when the line is perpendicular to the projection line, i.e., when $\vartheta = \varphi + 90^\circ$, which leads to

$$a = \tan(\vartheta - 90^\circ). \quad (\text{VI-6})$$

Now, if we take the Radon transform of the image for the specific angle $\vartheta = \varphi + 90^\circ$, we can estimate the offset parameter b from the position of its maximum value along the axis ρ . This position is indicated in Figure VI.2 as "C". Next, the offset parameter b can be computed as:

$$b = \frac{N_y}{2} + \frac{OC - \frac{N_x}{2} \sin(\vartheta - 90^\circ)}{\cos(\vartheta - 90^\circ)} = \frac{N_y}{2} + \frac{OC + \frac{N_x}{2} \cos(\vartheta)}{\sin(\vartheta)}, \quad (\text{VI-7})$$

where N_y is the length of the vertical side of the image, while N is the length of the horizontal side (in this case $N_x=N_y=256$). Note that the distance OC can be positive or negative and is actually negative in Figure VI.2.

Thus, the equation of the line can be determined by first applying the Radon transform of the image for angles between 0° to 180° , then finding the coordinates of the maximum point $(\vartheta_{max}, \rho_{max})$, as shown in Figure VI.3, and finally using equations (VI-6) and (VI-7) using $OC=\rho_{max}$ and $\vartheta=\vartheta_{max}$. Note that the accuracy of the estimates depends on the resolution of the image and the size of the angle step selected for the Radon transform. Unfortunately, any attempt to increase the resolution (size) or decrease the angle step results in increasing the computation load.

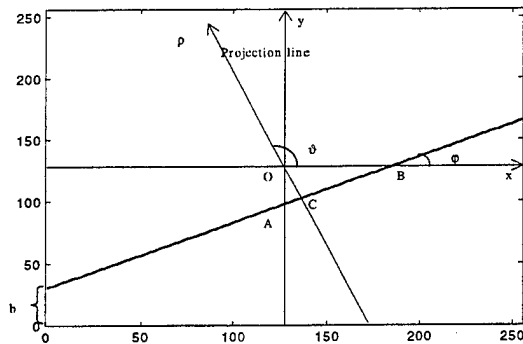


Figure VI.2: Radon transform geometry; image containing a single line.

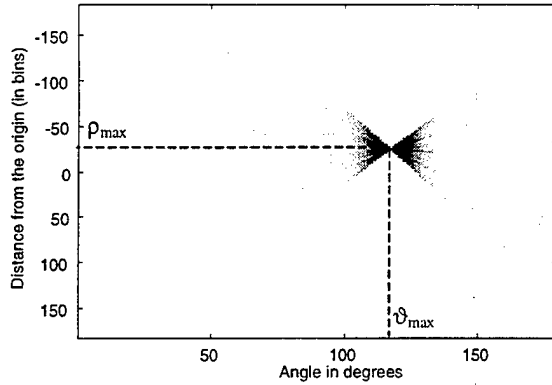


Figure VI.3: Radon transform for line shown in Figure VI.2; for $\vartheta=0^\circ, \dots, 180^\circ$, 1° inc.

To minimize the computational load we apply the Radon transform in two stages. First, we scan the image from 0° to 179° in steps of 2° . We determine the angle ϑ_{1m} that corresponds to the column that includes the point with the highest intensity. Next, we scan the image from the angle $\vartheta_{1m}-1^\circ$ to $\vartheta_{1m}+1^\circ$ in steps of 0.1° . Using this implementation allows the maximum line slope error to decrease to $\pm 0.05^\circ$ without having to cover the whole range of angles at that rate.

C. LINEARLY MODULATED CHIRPS

This section presents the scheme used to estimate linear chirp parameters. First, we present the method used to generate the signals. Next, we describe the image processing technique applied to extract the features from the time-frequency image. Finally, we compare the results obtained for each time-frequency representation considered and their robustness to noise degradations.

1. Signal Generation

The radar signals considered in this study are synthetic and consist of a train of several linearly modulated pulses, as shown in Figure VI.4.

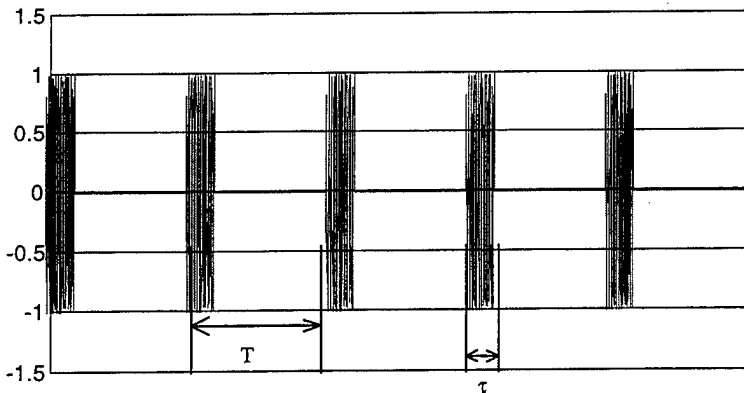


Figure VI.4: Synthetic radar signal; linear chirp modulation.

First, we assume that we can isolate one single pulse of duration τ . This extraction can easily be done with an energy detector in medium to high SNR levels. Thus, the received signal has an instantaneous frequency $f(t)$ defined as:

$$f(t) = f_0 + k \cdot t \quad (\text{VI-8})$$

Some of the time-frequency transformations considered in the study use the analytical version derived from the real received signal. In such cases, the analytical signal is computed with the Hilbert transform. The analytical noise-free linear chirp signal $s(t)$ is given as:

$$s(t) = e^{j2\pi(f_0t + \frac{k}{2}t^2)} \quad (\text{VI-9})$$

The signal is assumed to be sampled at a rate of 512 [samples/pulse length]. Recall that the sampling frequency for a real signal must be equal to at least twice its highest frequency component. Thus, the signal may be heterodyned down to a lower frequency if needed.

The discrete real part of the signal is given as:

$$s[n] = \operatorname{Re}(e^{j2\pi(\frac{f_0}{f_s} \cdot n + \frac{k}{2f_s^2} \cdot n^2)}) = \cos(2\pi(\frac{f_0}{f_s} \cdot n + \frac{k}{2f_s^2} \cdot n^2)), \quad n=1,..,512 \quad (\text{VI-10})$$

We can rewrite the above equation as:

$$s[n] = \cos(2\pi(f_{n0} \cdot n + \frac{a}{2} \cdot n^2)) \quad \text{where} \quad f_{n0} = \frac{f_0}{f_s}, \quad a = \frac{k}{f_s^2}, \quad n=1,..,512 \quad (\text{VI-11})$$

The terms a and f_{n0} represent the normalized slope and the normalized starting frequency respectively, with respect to the sampling frequency f_s . Thus, the normalized frequency equation for the linear chirp discrete signal is given by:

$$f_n = f_{n0} + a \cdot n, \quad n=1,..,512. \quad (\text{VI-12})$$

Normalizing the time index over the pulse length leads to the following normalized frequency equation for the linear chirp:

$$f_{nn} = f_{n0}/N + (a/N) \cdot n, \quad n=1,..,512.$$

Multiple linear chirp signals trials were generated by randomly selecting both the initial frequency and the slope. Note that sampling constraints need to be satisfied to avoid aliasing in the resulting discrete linear chirp. For example, the parameter a needs to be selected so that the final instantaneous frequency doesn't exceed 0.5 for a given initial

frequency f_{n0} . As a result, aliasing may be avoided by selecting both the initial and final normalized instantaneous frequencies within the range [0, 0.5], and computing the corresponding slope parameter a . Initial and final frequencies are selected from a uniform distribution defined in the range [0,0.5]. Next, the chirp is corrupted by additive white Gaussian noise. Analytical expressions needed to compute some of the time-frequency transformations are obtained with the Hilbert transform of the noisy signal. Real signal expressions were used to compute the wavelet-based decompositions.

2. Simulation Set-up and Extraction

The eleven different time-frequency and wavelet-based representations described in Section V were considered. The goal was to select a small number of transformations leading to the best “image quality” from that set. Recall that the representations considered were:

- Wavelet packet best basis,
- Cosine packet best basis,
- Wavelet pursuit,
- Cosine pursuit,
- Wigner-Ville distribution,
- Pseudo Wigner-Ville distribution (PWVD),
- Reassigned Pseudo Wigner-Ville distribution (Reassigned PWVD),
- Smoothed Pseudo Wigner-Ville distribution (SPWVD),
- Reassigned Smoothed Pseudo Wigner-Ville distribution (Reassigned SPWVD),
- Spectrogram,
- Reassigned spectrogram.

Figure VI.5 presents the image obtained for the various time-frequency representations considered for a linear chirp with SNR=10dB. A few comments are in order regarding the selection of the transform parameters.

1. Number of Atoms

Recall that defining a line in a plane requires two points only. However, these two points must be perfectly localized in both time and frequency, and must be immune from any noise interference. Theoretically, we could use two atoms only from an atomic decomposition to define the linear frequency equation. However, this doesn't hold in practice, as the atoms are not perfectly localized. Note that a larger number of atoms may better represent the line trend. However, some of the atoms may represent noise contributions for noisy signals. Therefore, selecting the number of atoms to represent a linear chirp in noise requires a trade-off between these two issues: fewer atoms to denoise the signal and more atoms to improve the resolution. We selected 10 atoms per decomposition for the atomic decompositions used in our study after running several trial cases.

2. Maximum Decomposition Level

Next, the maximum decomposition level was set to 7, as simulations showed no advantage in going to higher levels.

3. Wavelet Type

The mother wavelet function was selected after several trials among the readily provided functions in the Wavelab software [12]. Finally, we selected Daubechie-IV since it gave the best time-frequency representation for the types of signal considered.

4. Image Thresholding

No image intensity thresholding was applied to the time-frequency images, as simulations showed that it this step worsened the results for low SNR levels. Note that implicit denoising is actually performed by selecting a small number of atoms for the atomic decompositions.

5. Window Length

The PWV, SPWV and Reassigned SPWVD transformations use a frequency window which has a Hamming ($N/4$) time domain expression, and a Hamming ($N/10$) for time smoothing window. The analysis window selected for the spectrogram is Hamming ($N/4$), where N is the length of the signal (512 bins).

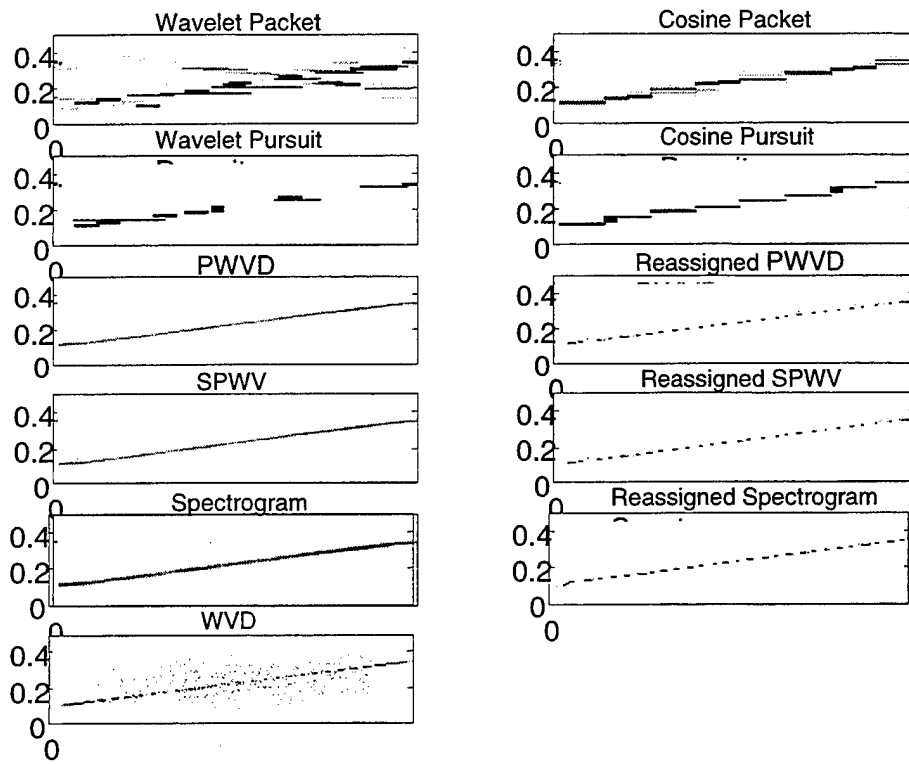


Figure VI.5: Various time-frequency representations for a linear chirp; SNR=10dB, Normalized frequency. Frequency normalized to sampling frequency.

6. Radon Transformation Implementation Issues

The Radon transform is selected to extract the line equation from the time-frequency image, as described earlier in Section VI.B. We use a two-stage implementation with final degree increment 0.1^0 . The size of the resulting image for each time frequency representation is set to 256x256 points, as the Radon transform for larger images would be too computationally expensive for a MATLAB implementation. One hundred randomly generated linear chirps for a given SNR level were generated, and the SNR varied in the range -10dB to 10dB . Next, the chirp parameters were estimated from

the images generated by each of the eleven time-frequency transformations considered. Performance comparisons are presented next.

3. Performance Results

3.a) Evaluation of Time-frequency Representations

Recall that the maximum theoretical slope error is $\pm 0.05^\circ$ since the final step angle in the radon transform is 0.1° , as discussed in Section V. However, we also have to add noise effects, and quantization errors introduced by the finite resolution in the image. Figures VI.7 to VI.9 present the mean and the standard deviation of the absolute slope and offset errors as a function of the SNR level for all time-frequency transformations considered in the study. Figure VI.6 represents an idealized image which could be obtained with a time-frequency transformation. Note that the frequency axis is normalized by the sampling frequency, and the time axis is normalized by the pulse length. Thus, the chirp slope parameter expressed in degrees is given by:

$$\alpha = \frac{180}{\pi} \tan^{-1}(f_1 - f_0),$$

and the offset value expressed in number of (frequency) bins is given by:

$$f_{n0} = f_0 \times 512,$$

where f_0 and f_1 respectively represent the normalized starting and ending chirp frequencies. The offset value is multiplied by the length of the frequency transformation used.

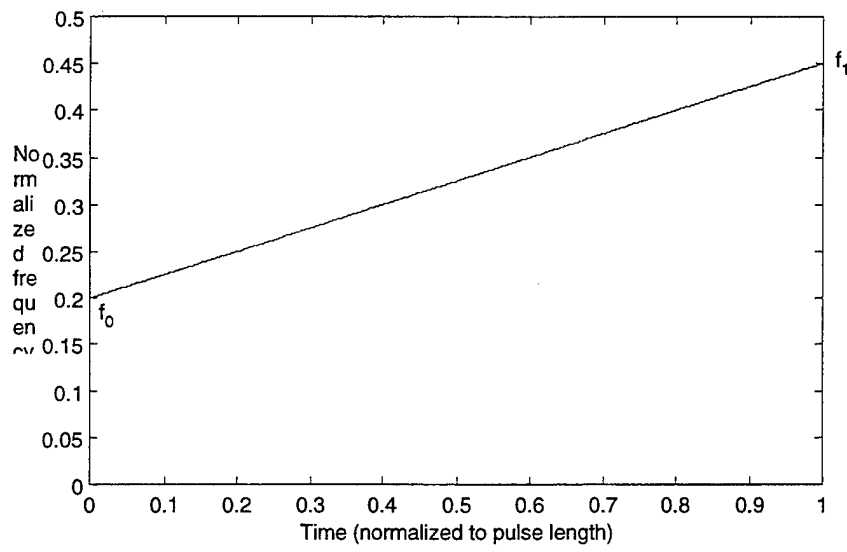


Figure VI.6: Time-frequency image for a linear chirp; normalized frequency ($f_s = 1$), starting frequency $f_0 = .2$ and ending frequency $f_1 = 0.4$

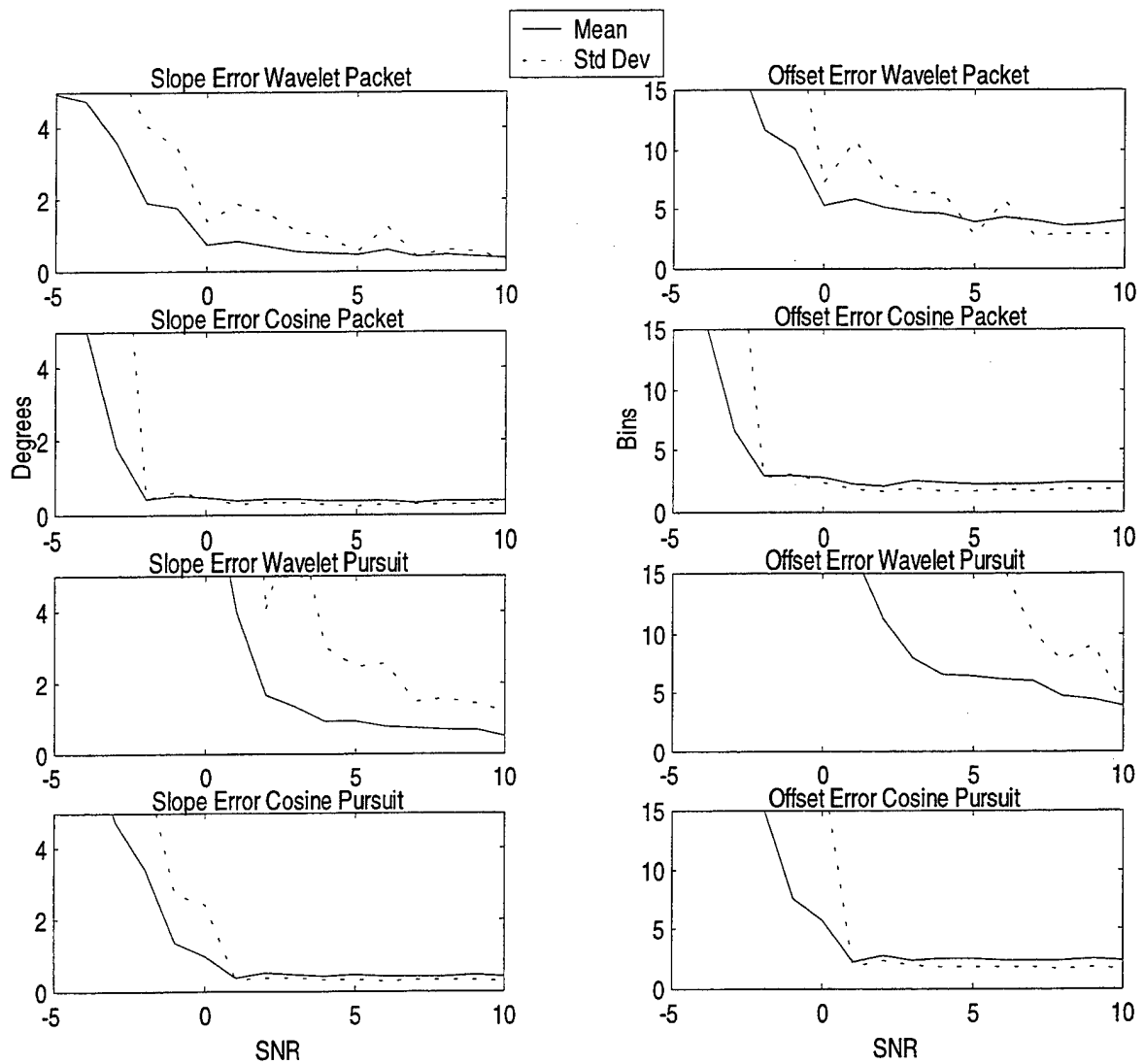


Figure VI.7: Slope and offset errors for wavelet and cosine packet, wavelet and cosine pursuit decompositions for linear chirp signals; SNR given in dB.

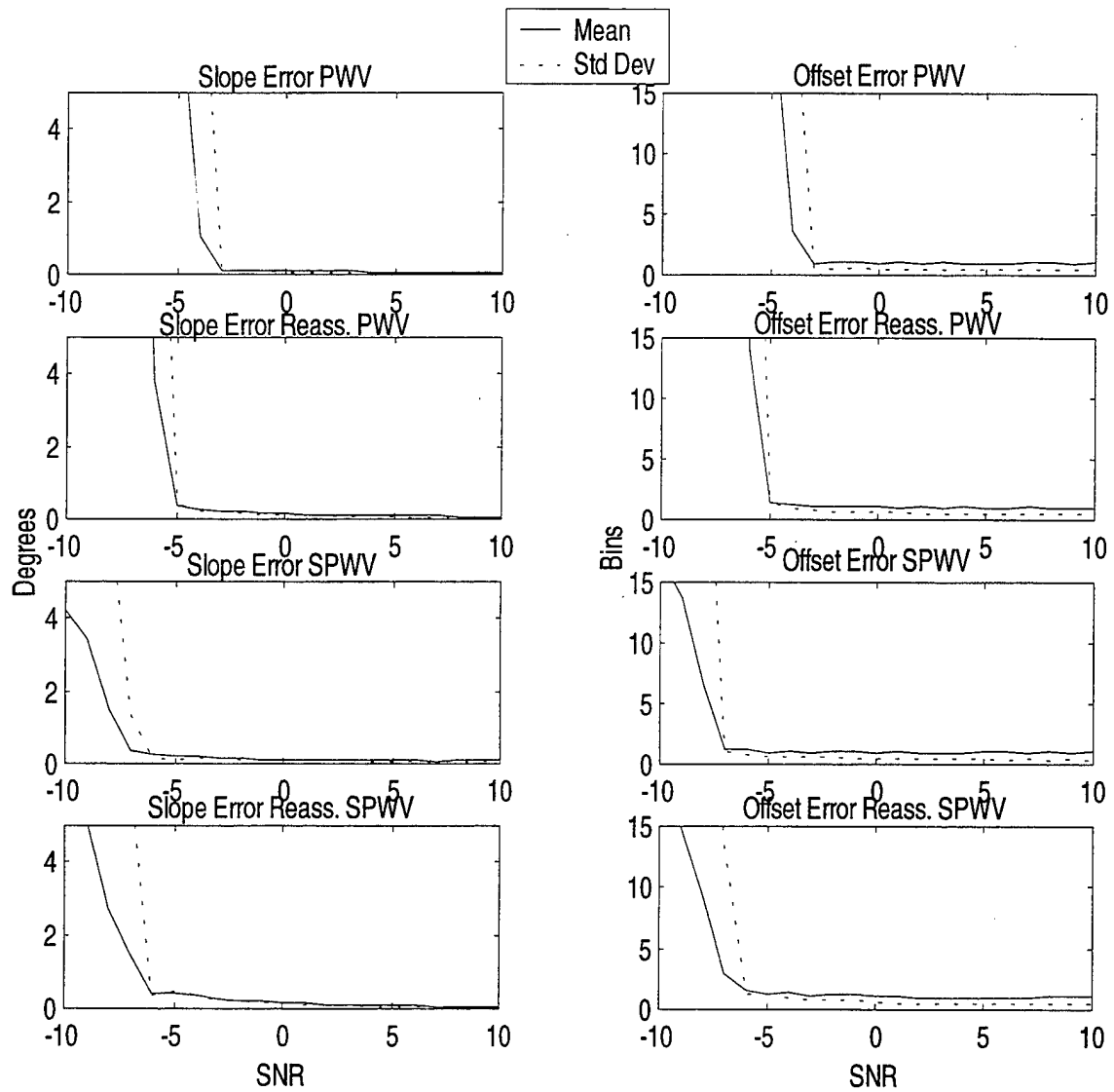


Figure VI.8: Slope and offset errors for the PWV, reassigned PWV, SPWV, and reassigned SPWV decompositions; linear chirp signals; SNR given in dB.

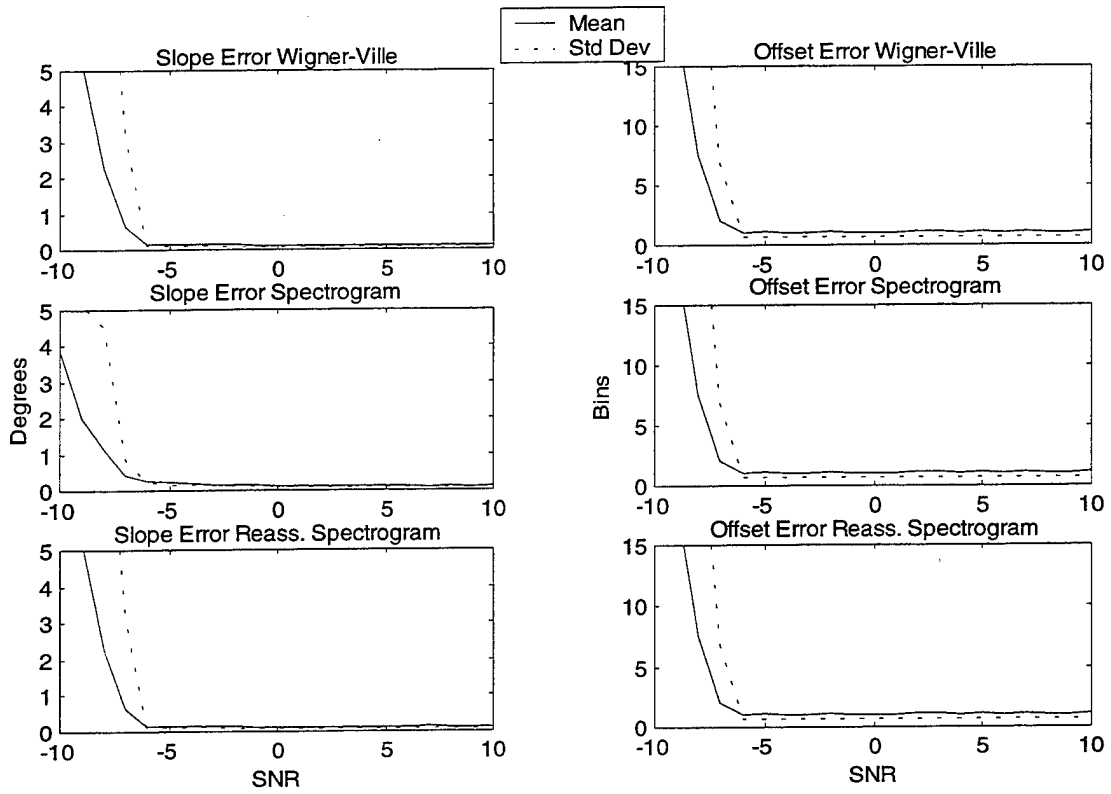


Figure VI.9: Slope and offset errors for the Wigner-Ville decomposition, Spectrogram, and reassigned Spectrogram; linear chirp signals; SNR given in dB.

A few comments are in order:

1. Results show that all the energy distributions perform better than the atomic (i.e., wavelet-based) decompositions. This is to be expected as they provide a more accurate “image” in the time-frequency plane. Note that atoms cannot be well localized in both time and frequency, as would be required to represent linear chirps accurately. The best-basis cosine packet decomposition gives the best results followed by the cosine pursuit scheme for atomic decompositions.

2. Most of the energy distributions have slope errors very close to the theoretical value of 0.05° for medium to high SNR levels. All transformations show a SNR level breaking point at which the errors suddenly increase. This is to be expected as the extraction relies on the quality of the TFR. Figures VI.10 and VI.11 illustrate the degradation which may occur in the TFR image quality at $\text{SNR}=-10\text{dB}$ and the corresponding parameter estimation results.
3. The Wigner-Ville distribution has a very good and almost stable performance for SNR's in the range of -6dB to 10dB . The smoothing time window present in the Pseudo Wigner-Ville distribution improves the estimation in higher SNR but shrinks the effective range. The Smoothed Pseudo Wigner-Ville distribution has a slightly worst performance at high SNR but also has the widest effective range. The smoothing in time and in frequency eliminates the interference terms almost completely so that the representation is more immune to the noise than other transformations are. However, frequency smoothing results in lowered performance at high SNR levels.
4. Results show that the reassign method usually improves the performance at high SNR levels, as it forces the representations to be more "focused". Unfortunately, applying the reassigned method in low SNR levels worsens the performances. This is to be expected as the presence of noise close to the line moves the local center of gravity of the distribution away from its theoretical value.

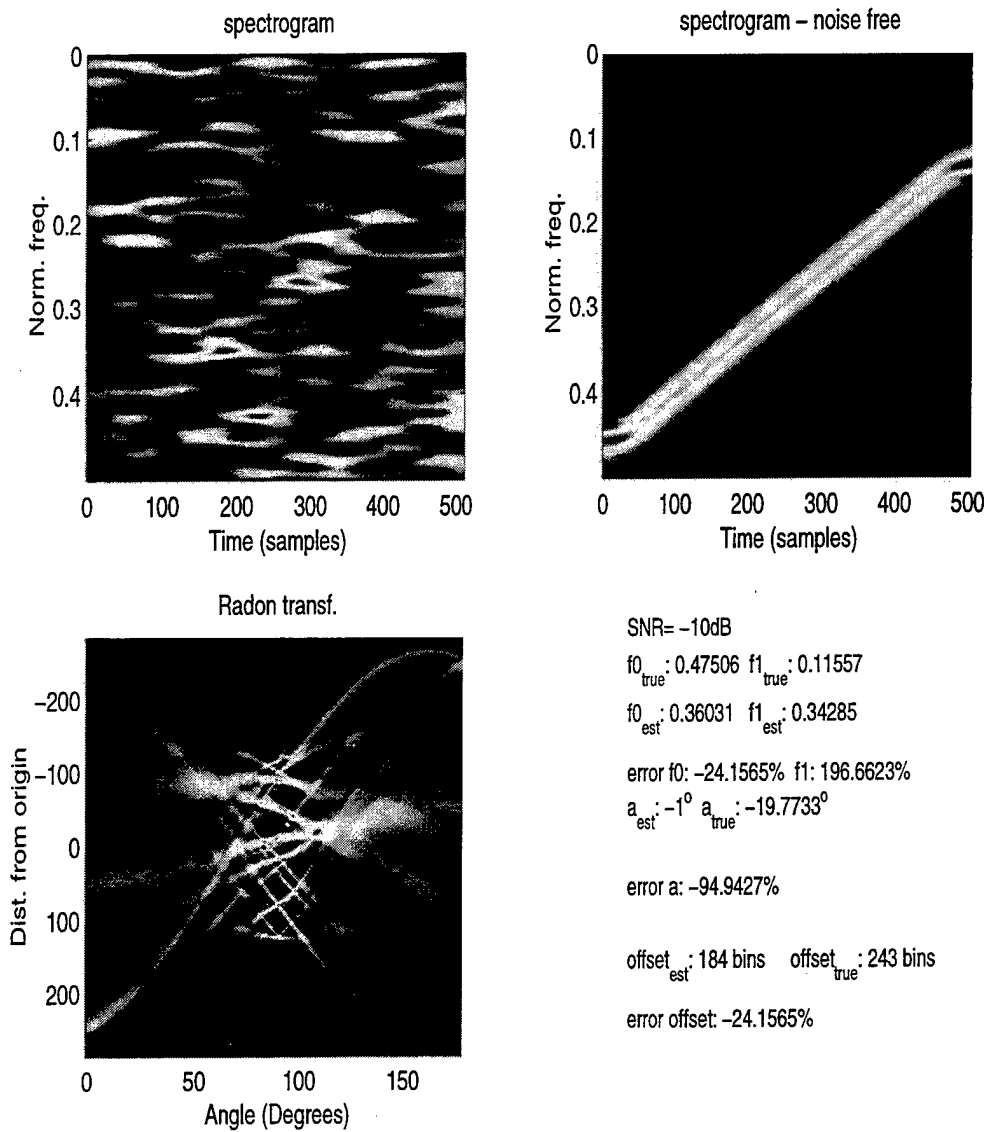


Figure VI.10: Linear chirp trial case 1; SNR=-10dB; true and estimated modulation parameters.

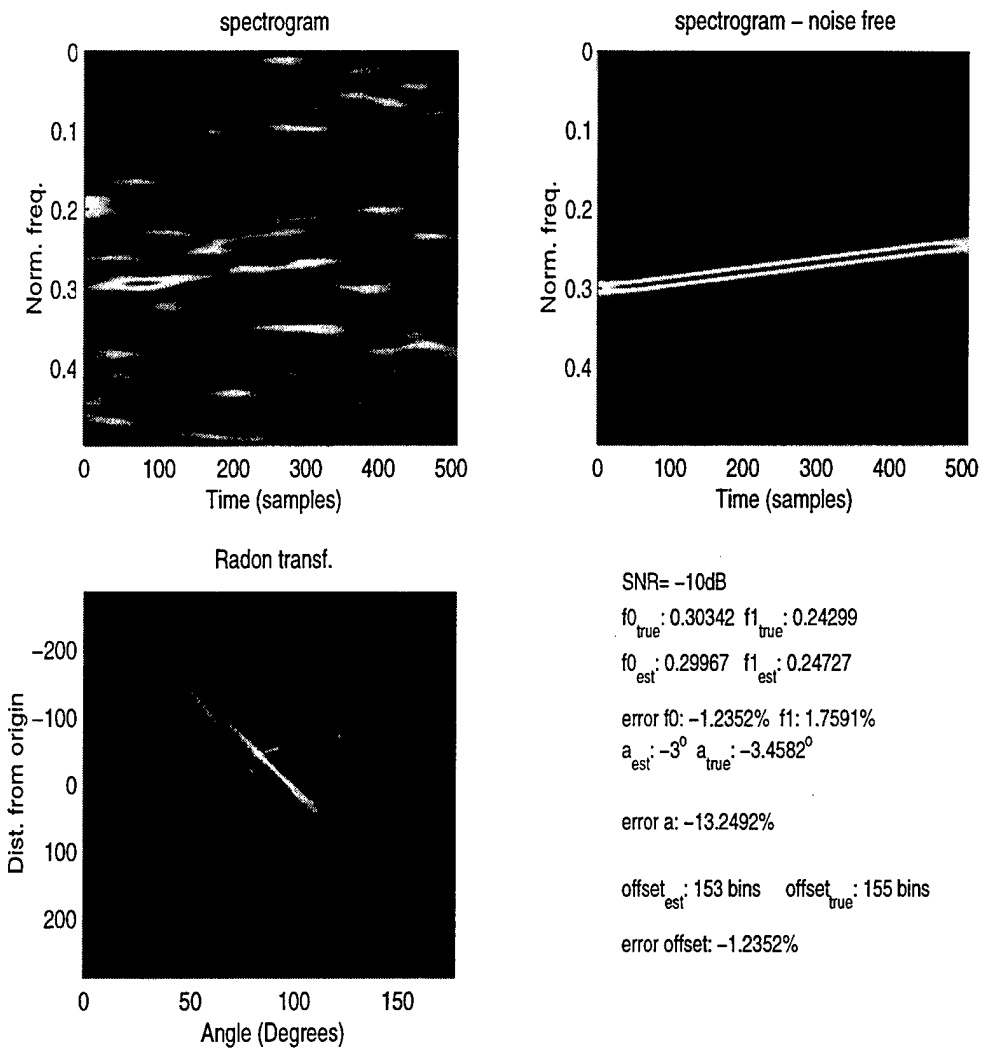


Figure VI.11: Linear chirp trial case 2; SNR=-10dB; true and estimated modulation parameters.

Table VI.1 lists the mean absolute error for the frequency slope and offset parameters at SNR equal to 10dB for all transformations considered for a “rough” comparison of the transformation performances. In addition, Table VI.1 lists the SNR level at which the errors suddenly increase, indicating the SNR level at which using a specific distribution may become more questionable.

	Mean of absolute slope error @ SNR=10dB (in degrees)	Mean of absolute offset error @ SNR=10dB (in bins)	Breaking point (in dB)
Wavelet Packet	0.375	4	0
Cosine Packet	0.5149	3.98	0
Wavelet Pursuit	0.37	2.35	4
Cosine. Pursuit	0.4297	2.35	0
WV	0.1198	1.08	-7
PWV	0.0623	1.02	-4
Reassigned PWV	0.0729	1	-5
SPWV	0.0792	1.02	-7
Reassigned SPWV	0.0563	1.02	-7
Spectrogram	0.098	1.77	-7
Reassigned Spectrogram	0.12	1.78	-7

Table VI.1: Mean absolute errors for frequency slope and offset. 100 trials, SNR=10dB, performance breaking points for all time-frequency methods considered.

3.b) Error Evaluation

Recall the received signal was sampled at a rate of 512 [samples/pulse period] while the image size was set to 256x256 bins in order to speed up the computations. However, the errors presented were corrected to correspond to an image with size 512x256, where the time and frequency axes have 512 and 256 bins respectively. Next, the goal is to investigate how the estimated errors relate to the frequency error obtained for the frequency expression given in equation (VI-8).

Recall that the normalized frequency expression is given by:

$$f_n = f_{n0} + a \cdot n ,$$

and the slope angle ϑ measured in the image is:

$$\tan(\vartheta) = \frac{a \cdot N \cdot 2N_f}{N_t}, \quad (\text{VI-12})$$

where a is the frequency slope parameter, N is the length of the signal, and N_f and N_t represent the number of bins in the frequency and time axis respectively. In our case $N_f=N/2$ and $N_t=N$. Thus, equation (VI-12) simplifies to:

$$\tan(\vartheta) = a \cdot N . \quad (\text{VI-13})$$

Recall that

$$s[n] = \cos(2\pi(f_{n0} \cdot n + \frac{a}{2} \cdot n^2)), \text{ where } f_{n0} = \frac{f_0}{f_s}, \quad a = \frac{k}{f_s^2}, \quad n=1,..,512$$

Let's assume that the linear chirp has frequency slope k_0 and that ϑ_0 is the corresponding angle, which leads to:

$$\frac{k_0}{f_s^2} = a_0 = \frac{\tan(\vartheta_0)}{N}. \quad (\text{VI-14})$$

Now, let's assume we estimate an angle equal to ϑ_{est} instead of ϑ_0 due to errors in the estimation process. Thus,

$$\vartheta_{est} = \vartheta_0 + \Delta\vartheta, \quad (\text{VI-15})$$

where $\Delta\vartheta$ is the angle error. As a result, the resulting estimated frequency slope k_{est} expression is given by:

$$\begin{aligned} k_{est} &= f_s^2 \cdot a_{est} = f_s^2 \cdot \frac{\tan(\vartheta_0 + \Delta\vartheta)}{N} \\ &= \frac{f_s^2}{N} \cdot \frac{\tan(\vartheta_0) + \tan(\Delta\vartheta)}{1 - \tan(\vartheta_0) \cdot \tan(\Delta\vartheta)} \\ &= \frac{k_0 \cdot f_s^2 \cdot N + f_s^4 \cdot \tan(\Delta\vartheta)}{f_s^2 \cdot N - k_0 \cdot N^2 \cdot \tan(\Delta\vartheta)}. \end{aligned} \quad (\text{VI-16})$$

Thus, the final frequency slope error is:

$$\Delta k = k_0 - k_{est} = \frac{(k_0^2 \cdot N^2 + f_s^4) \cdot \tan(\Delta\vartheta)}{k_0 \cdot N^2 \cdot \tan(\Delta\vartheta) - f_s^2 \cdot N}. \quad (\text{VI-17})$$

The slope frequency error Δk is expressed in terms of the angle error, but also depends on the sampling frequency, and the length of the signal N .

If we assume again that f_0 is the initial offset value corresponding to equation (VI-8), then the normalized offset frequency is derived from equation (VI-11) as $f_{n0}=f_0/f_s$. The value f_{b0} measured is expressed in bins and is related to f_{n0} by:

$$f_{b0} = f_{n0} \cdot 2 \cdot N_f \quad (\text{VI-18})$$

Assume the estimated initial offset value f_{best} contains an error Δf_b . Thus,

$$f_{best} = f_{b0} + \Delta f_b , \quad (\text{VI-19})$$

and the estimated value for f_0 according to equations (VI-11) and (VI-8) is given by:

$$f_{0est} = f_s \cdot \frac{f_{b0} + \Delta f_b}{2N_f} = f_0 + f_s \cdot \frac{\Delta f_b}{2N_f} . \quad (\text{VI-20})$$

When $N_f=N/2$, the resulting error is:

$$\Delta f_0 = f_0 - f_{0est} = -f_s \cdot \frac{\Delta f_b}{N} . \quad (\text{VI-21})$$

Equations (VI-17) and (VI-21) provide the relations between errors measured in the time-frequency image representation of size $N/2 \times N$, where N is the length of the signal, and the corresponding errors in the initial time-varying frequency expression given in Equation (VI-8). Note that Δf_b is measured in bins.

3.c) Multi-pulse processing results

Up to this point, all results were derived by extracting the frequency modulation parameters from one noisy radar pulse. Performances improve when using more than one pulse. Assume we isolate five radar pulses, where each pulse contains the same transmitted signal at a given SNR level. Note that the signal information gets mapped to the same location of the time-frequency plane, while the noise contributions scatter to different location in each trial. Thus, averaging multiple time-frequency images improves the quality of the signal information.

Thus, averaging the contribution of five pulses leads to the results shown in Figure VI.12 obtained for the Smoothed Pseudo Wigner-Ville transformation. One hundred realizations per SNR level are used, and SNR levels varied from -20 to 0dB. Note that there is no need to consider higher SNR levels as the error curves already flatten for SNR=0dB. Results show a significant improvement over using one pulse only. Further improvements may be obtained by considering a larger number of pulses. However, this will result in a direct increase of the computation time.

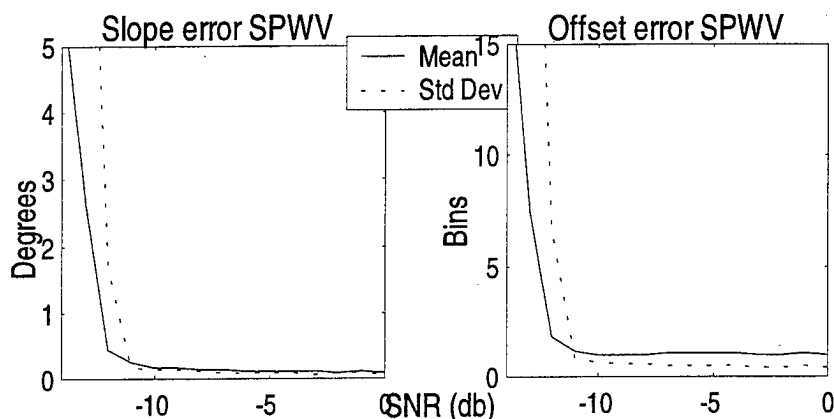


Figure VI.12: Slope and offset error for the SPWV distribution; five realizations.

3.d) Application to the AN/SPS-40B radar

We apply the above results to a specific radar using pulse compression readily available to us: the SPS-40B radar. The Radar Set AN/SPS-40B is used for the detection

ranging and tracking of air targets at long range in American and foreign navy services [24]. In this pulse mode, the pulse length is $\tau=60\mu\text{sec}$. The transmitted waveform inside the pulse is a linear modulated down-chirp with a bandwidth of 2MHz centered at a frequency that can be varied manually by the operator from 402.5 to 447.5 MHz.

Let's assume that the radar operates at 437.5 MHz, i.e., the chirp starts with a frequency 438.5MHz and decays linearly to 436.5 MHz. Our ESM (Electronic Support Measures) receives a series of noisy pulses from this radar. Further, assume we can isolate one pulse perfectly and that the estimated received signal is centered at 438MHz with a bandwidth equal to 2MHz. Given that the duration of the pulse is $60\mu\text{sec}$ and if we use 512 [samples/pulse duration], the sampling frequency should be set at:

$$f_s = \frac{512}{60} \text{MHz} = 8.53 \text{MHz}. \quad (\text{VI-22})$$

This sampling frequency does not satisfy the Nyquist rate. Thus, we can either increase the sampling frequency or heterodyne to a lower center frequency. The first option has the drawback of increasing the number of samples to deal with, and the computational load of the estimation schemes considered. Heterodyning the signal down to the baseband can be accomplished by multiplying the received signal with a cosine function, and using a lowpass filter to extract the information. Assume the heterodyning frequency is selected as 440MHz. Thus, the resulting chirp signal is an up-chirp at the frequency $440-437.5=2.5\text{MHz}$ with bandwidth equal to 2MHz after heterodyning and filtering. The theoretical time-frequency representation is shown in Figure VI.13. Thus, the instantaneous frequency of the heterodyned signal is given by:

$$f(t) = 1.5 \cdot 10^6 + 3.33 \cdot 10^{10} \cdot t. \quad (\text{VI-23})$$

The heterodyned signal may be sampled with a frequency $f_s=8.53\text{Mhz}$, corresponding to 512 samples/pulse duration.

Assume we use the SPWV distribution and the chirp parameter estimation procedure described above in Section V-B. Figure VI.12 shows that the mean slope error is 0.09° and the mean offset error is 1 bin when the SNR is equal to 5dB. Using equations (VI-17) and (VI-21) leads to:

$$|\Delta k|=2.610^8 \text{ and } |\Delta f_0|=1.6710^4,$$

meaning that the normalized errors for the frequency slope and offset are equal to

$$\frac{|\Delta k|}{3.33 \cdot 10^{10}} = 0.008 \text{ or } 0.8\% \text{ and } \frac{|\Delta f_0|}{1.2 \cdot 10^6} = 0.0104 \text{ or } 1.04\% \text{ respectively for the}$$

heterodyned signal.

Note that the normalized slope error remains the same for the original received signal, as the signal bandwidth has not been changed by the heterodyning process, while the normalized frequency offset error becomes equal to $1.6710^4/438.510^6$, i.e., 0.0038%.

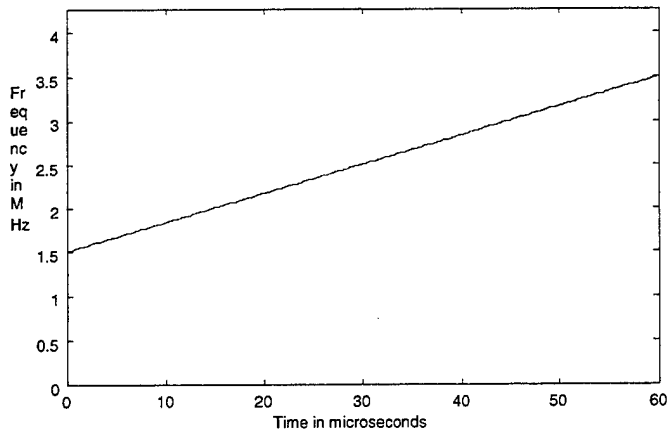


Figure VI.13: Instantaneous frequency for the heterodyned signal; Normalized frequency $f_s = 1$.

4. Comparisons

Other schemes extracting the modulation parameters have been proposed in the literature with their own advantages and drawbacks [25-33]. In this section, we consider the scheme proposed by Peleg and Porat which estimates the parameters of a complex linear FM scheme from a finite number of noisy observations

$x[n] = s[n] + w[n], n = 1, \dots, N$, where $w[n]$ is white noise and $s[n]$ is a linear chirp signal defined as:

$$s[n] = \cos(2\pi(f_{n0}n + \frac{a}{2}n^2)), n = 1, \dots, N,$$

which leads to the following normalized time-varying frequency for the chirp:

$$f_n = f_{n0} + an, n = 1, \dots, N.$$

4.a) Introduction

Peleg and Porat proposed a fast estimation scheme based on two FFT operations and two one-dimensional searches of the resulting FFT quantities [25]. The scheme uses the fact that the maximum likelihood estimates of the parameters of a complex linear FM signal can be derived by the two-dimensional maximization of the maximum likelihood function $L(a, f_{n_0})$ defined as:

$$L(a, f_{n_0}) = \left| \sum_{n=1}^N x_n \exp\left(-\frac{ja^2 n}{2} + f_{n_0} n\right) \right|^2.$$

Peleg and Porat proposed to replace the two-dimensional maximization operation by two successive one-dimensional maximization searches to obtain a sub-optimal solution obtained with the following steps:

- 1) Compute the discrete form of the ambiguity function $DAF(x, \omega, n_0)$ defined as:

$$DAF(x, \omega, n_0) = \sum_{n=1}^{N-n_0} x_{n+\tau} x_n^* e^{-j\omega n},$$

The parameter n_0 is chosen equal to $N/2$, as this value minimizes the mean square error of the slope parameter a as a function of n_0/N , as shown by Peleg and Porat [25].

- 2) Find the frequency ω_{\max} which maximizes the magnitude of $DAF(x, \omega, n_0)$, leading to

$$\bar{a} = \frac{\omega_{\max}}{n_0}.$$

- 3) Define:

$$z_n = x_n e^{(-j\bar{a}n^2)}, n = 1, \dots, N.$$

- 4) Compute the parameter $\overline{f_{n_0}}$ which maximizes $L(\omega, \bar{a})$ with respect to ω :

$$L(\omega, \bar{a}) = |DFT(z_n, \omega)|^2 = \left| \sum_{n=1}^N z_n e^{-j\omega n} \right|^2.$$

Peleg and Porat showed that their scheme approaches CRB values for SNR values above 5dB. They also indicated that the SNR level should satisfy the following constraint for a given number of data points:

$$SNR \geq \frac{1}{N} (50 + \sqrt{2500 + 50N})$$

where N represents the data length, for the results to be meaningful [25].

4.b) Simulations

We generated one hundred linear chirps of length 512 samples with random start and stop normalized frequencies in the range [0, .5] for a given SNR level. The SNR was varied in the -10dB to 10dB in steps of 2dB, as done previously in Section VI.C.3, and the chirp parameters estimated following the scheme proposed by Peleg and Porat. Figure VI.14 presents the results obtained. We compared the results obtained for our best three transform types (Pseudo Wigner-Ville, reassigned pseudo Wigner-Ville, and reassigned smoothed Pseudo Wigner-Ville distributions) to those obtained by Porat and Peleg. Results show that the Porat and Peleg scheme:

- 1) starts to break down around -7dB, and
- 2) is not as robust to noise degradations as those based on combined TFR/Radon transforms as the estimation errors are significantly larger for SNRs below – 5dB.

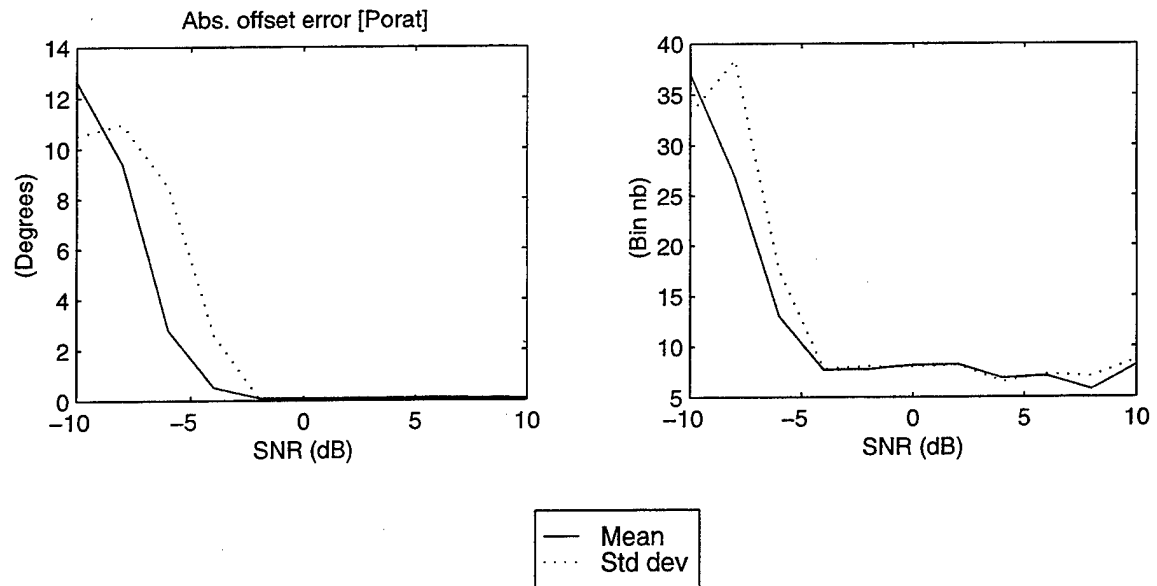


Figure VI.14: Slope and offset errors obtained with Peleg and Porat' scheme; linear chirp signals [25]; 100 trials per SNR level; left plot: slope error; right plot: offset error.

VII. HYPERBOLIC CHIRP PARAMETERS ESTIMATION

This section considers the estimation of hyperbolic chirp parameters. As before, the starting point is the time-frequency image representation of the information. However, generalizations of the Radon transform to hyperbolic line types were not used. Instead, we consider an iterative procedure to estimate the chirp parameters.

Note that we assume we know the type of modulation transmitted, as we do not address issues related to distinguishing between linear and hyperbolic modulation types. Such classification issues are left for future work.

A. SIGNAL GENERATION

1. Introduction

Assume that we can isolate individual pulses of duration $\tau=512$ samples. Thus, a received signal with hyperbolic modulation frequency is given by:

$$x(t) = \cos(2\pi(A \ln(t + t_0) + B \cdot t)), \quad (\text{VI-1})$$

where

$$f(t) = \frac{A}{t + t_0} + B. \quad (\text{VII-2})$$

The analytical signal $s(t)$ obtained from $x(t)$ with a Hilbert transform is given by:

$$x(t) = e^{j2\pi(A \ln(t + t_0) + Bt)}. \quad (\text{VII-3})$$

The corresponding discrete signal $x[n]$ is given by:

$$x[n] = e^{j2\pi(A \cdot \ln(\frac{n}{f_s} + \frac{n_0}{f_s}) + B \cdot \frac{n}{f_s})} = e^{j2\pi(A \cdot \ln(n + n_0) - A \cdot \ln(f_s) + \frac{B}{f_s} \cdot n)}, \quad (\text{VII-4})$$

or finally

$$x[n] = K \cdot e^{j \cdot 2\pi(a \cdot \ln(n+n_0) + bn)}, \quad (\text{VII-5})$$

where:

$$a = A, \quad b = \frac{B}{f_s}, \quad n_0 = f_s \cdot t_0, \quad \text{and} \quad K = e^{j2\pi A \ln(f_s)}. \quad (\text{VII-6})$$

The normalized instantaneous frequency expression is given by:

$$f_n[n] = \frac{a}{n+n_0} + b. \quad (\text{VII-7})$$

Recall that we need to select the parameters a , b and n_0 such that the range of the normalized frequency $f_n[n]$ is between 0 and 0.5 to prevent aliasing, which leads to the following ranges:

$$a \in [0, \infty], \quad n_0 \in [0, \infty], \quad b \in [-\infty, 0.5] \quad (\text{VII-8})$$

A valid selection for a , b and n_0 is obtained by selecting one parameter in its allowed range, and then the other two so that they also fall in their allowed ranges. In the simulation, we first select a value for b from a uniform distribution in the region $[0, 0.5]$. The starting frequency at $n=0$, $f_n(0)$, is selected from a uniform distribution in the region $[b, 0.5]$. The final frequency $f_n(N)$, for $n=N$, where N is the signal length, can be selected in the range $[b, f_n(0)]$. Defining b , $f_n(0)$, and $f_n(N)$ leads to the following values for a and n_0 :

$$a = \frac{(f_n(0) - b) \cdot (b + f_n(0)) \cdot N}{(f_n(0) - f_n(N))} \quad (\text{VII-9})$$

$$n_0 = \frac{(b + f_n(N)) \cdot N}{(f_n(0) - f_n(N))}. \quad (\text{VII-10})$$

Note that this random selection can sometimes lead to a frequency equation with a very steep slope at the beginning, as shown in Figure VII.1. Such a behavior is undesirable because none of the time-frequency representations gives good resolution in the area of the steep slope, and this modulation type is not typical in radar applications.

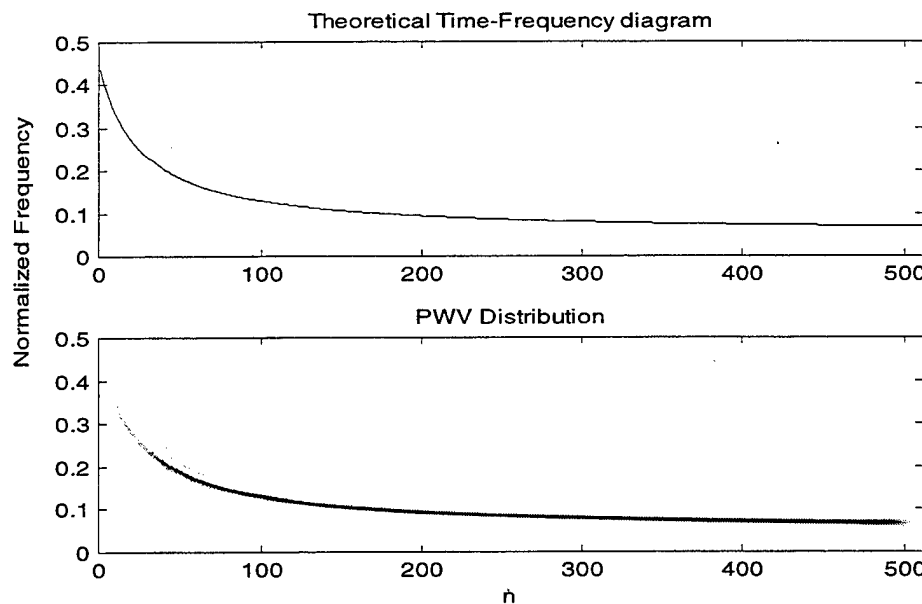


Figure VII.1: Hyperbolic modulation; normalized frequency for $a=10$, $n_0=25$, $b=0.05$.

2. Hyperbolic Line Parameter Constraints

We wish to restrict our random selection of the signal parameters to those leading to chirps without steep slopes, and need to automate the process so that we can run multiple trials to study the scheme robustness to noise degradations. Thus, we define a figure of merit that describes the amount of curvature present in a given hyperbolic line.

The parameter selected to characterize the curvature of the chirp is the distance d defined as the maximum distance between any point of the curve and its cord.

Note the parameter b shifts the hyperbolic chirp up or down without affecting the shape, thereby its curvature. Therefore, we assume that $b=0$ for simplicity. In such a

case, the chord associated to the hyperbolic chirp $f_n[n] = \frac{a}{n+n_0}$ is a line passing through

the points $(0, \frac{a}{n_0})$ and $(N, \frac{a}{N+n_0})$ with equation:

$$\frac{f - \frac{a}{n_0}}{n - 0} = \frac{\frac{a}{N+n_0} - \frac{a}{n_0}}{N - 0}.$$

The resulting chord equation is given by:

$$a \cdot n + n_0 \cdot (N + n_0) \cdot f - a \cdot (N + n_0) = 0, \quad (\text{VII-11})$$

which leads to:

$$f = \frac{-a}{n_0 \cdot (N + n_0)} n + \frac{a}{n_0}. \quad (\text{VII-12})$$

Recall that the gradient of a curve at a given point is a line that passes through that point and has a slope equal to the derivative of the curve at that point. Thus, the gradient at any point of the hyperbolic line is:

$$A = f' = \frac{-a}{(n + n_0)^2}. \quad (\text{VII-13})$$

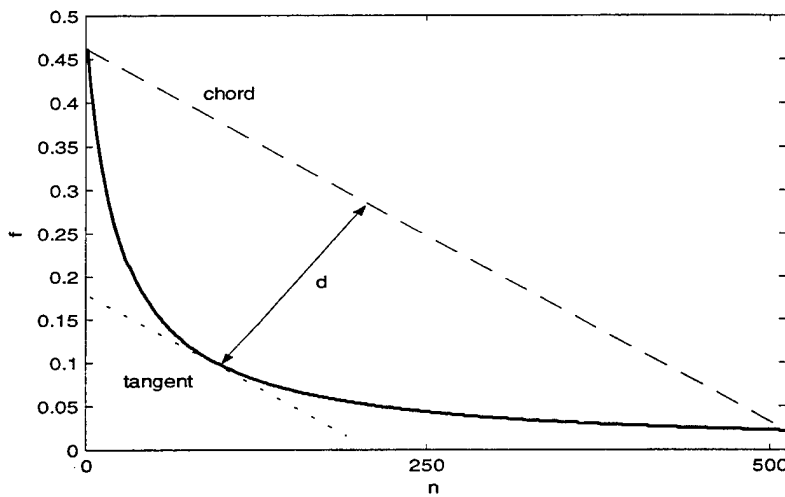


Figure VII.2: Maximum distance between a hyperbolic line and its chord; $a=12$, $n_0=25$, $b=0$.

The distance d is maximum at the point $n=\xi$ where its gradient is parallel to the chord. As a result, the gradient slope at the point $n=\xi$ is equal to the slope of the chord. Thus the position of the point $n=\xi$ can be estimated from (VII-11) and (VII-13) as:

$$\frac{-a}{(\xi + n_0)^2} = \frac{-a}{n_0 \cdot (N + n_0)},$$

which yields the coordinates of the point ξ as:

$$\xi = \sqrt{n_0(N + n_0)} - n_0, \quad (\text{VII-14})$$

$$f(\xi) = \frac{a}{\sqrt{n_0(N + n_0)}}. \quad (\text{VII-15})$$

Recall the distance d between a point (x_1, y_1) and a line with equation $a_1 \cdot x + a_2 \cdot y + a_3 = 0$ is given by the equation:

$$d = \frac{|a_1 \cdot x_1 + a_2 \cdot y_1 + a_3|}{\sqrt{a_1^2 + a_2^2}}. \quad (\text{VII-16})$$

Thus, the distance between the chord and the point $(\xi, f(\xi))$ can be computed using equations (VII-11), (VII-14), (VII-15), and (VII-16), which leads to:

$$d = \frac{|a \cdot \xi + n_0 \cdot (N + n_0) \cdot f(\xi) - a \cdot (N + n_0)|}{\sqrt{a^2 + n_0^2(N + n_0)^2}},$$

and:

$$d = \frac{|a| \cdot |(N + 2 \cdot n_0) - 2 \cdot \sqrt{n_0(N + n_0)}|}{\sqrt{a^2 + n_0^2(N + n_0)^2}}. \quad (\text{VII-17})$$

The distance d can be viewed as a figure of merit for the curvature of the hyperbolic line. A high value of d means the curvature is high and the time-frequency representation near the time origin is poor. However, very small values of d represent cases for which the hyperbolic curve is almost indistinguishable from a straight line. Thus, we restricted the chirp signals generated so that the distance d is in the region $\left[\frac{20}{1024} \cdot f_s, \frac{80}{1024} \cdot f_s \right]$ to avoid such cases.

Next, additive zero-mean white Gaussian noise is added to generate the noisy chirp with a specific SNR level.

B. FEATURE EXTRACTION

1. Introduction

The signal time-frequency representation can be obtained with any of the energy distributions discussed earlier in Section V. However, note that the atomic

decompositions are not as well suited as the energy distributions for the task at hand, as they do not describe the hyperbolic line curvature accurately. Therefore, we only consider energy distributions in this chapter.

At this point the task is to extract the three unknowns parameters (a, b, n_0) for a given time-frequency representation. The basic Radon transform can no longer be applied, as it is defined for straight lines only. The Radon transform was extended to detect functions of arbitrary shape [17], however the computational load is significantly higher.

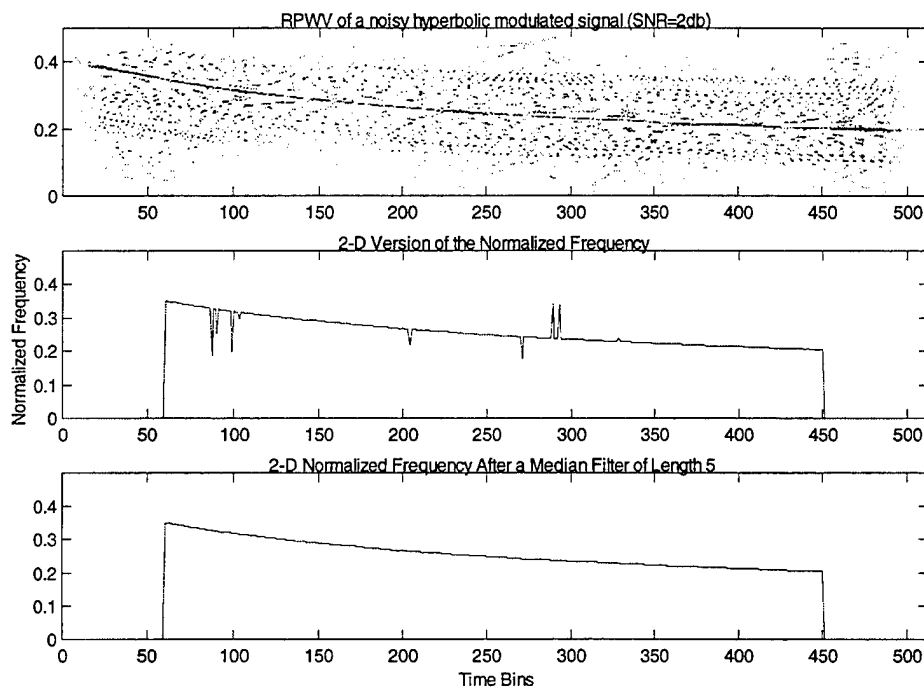


Figure VII.3: Extraction of the instantaneous normalized frequency expression from the time-frequency image. Before and after median smoothing, $L=5$.

The method considered here approaches the problem quite differently. It is an adaptive procedure which fixes one of the three unknown parameters at each iteration, and estimates the other two. The resulting scheme is presented next.

2. Method Description

The instantaneous frequency expression for the hyperbolic chirp is extracted from the two-dimensional image by selecting the peak values obtained at each time bin of the image. The result is a vector containing the frequency values for each time bin, as shown in Figure VII.3.

Note that the 2-D instantaneous frequency approximation is very accurate at high SNR levels, and degrades as the SNR level decreases. In noisy environments, the pixel with the highest energy obtained at a given time bin may be an outlier, resulting in spikes in the instantaneous frequency estimate, as illustrated in the middle plot of Figure VII.3. Such outliers can be smoothed out with a median filter. Simulations showed that a median filter of length 5 smoothed out potential “spikes” without loss of resolution.

We selected the three energy transformations leading to the best time-frequency image quality for the linear chirp case, and restricted our hyperbolic chirp analysis to those. The distributions selected are:

- Pseudo Wigner-Ville distribution,
- Reassigned Pseudo Wigner-Ville distribution,
- Reassigned Smoothed Pseudo Wigner-Ville distribution.

We set the dimension of the image at 512x512 bins to increase the image resolution and reduce quantization errors. In addition, simulations showed that these three

energy distributions do not necessarily perform well at the beginning and end of the image. As a result, we only consider the image from time bin 60 to time bin 450.

The second step in the proposed scheme approximates the instantaneous frequency adaptively with a hyperbolic line by minimizing the squared error between the information contained in the image and a theoretical hyperbolic curve expression. Note that the problem to be solved is non-linear, due to the specific frequency law to be approximated, as we estimate the parameters a , b and n_0 given in equation (VII-7). We first tried to solve the problem using a classical nonlinear least square iteration scheme provided with the function “lsqnonlin” from the MATLAB optimization toolbox [15]. Simulations showed that the algorithm converged to different local minimum, depending on the initial values selected. However, this problem can be resolved using a two-step procedure as follows.

Assume we wish to approximate the hyperbolic curve given in equation (VII-7) with a function of the form:

$$y(n) = \frac{a}{n + n_0}. \quad (\text{VII-18})$$

If we assume our estimation values obtained from the image to be equal to $y_{est}(n)$, $n=1,\dots,N$, then we wish to find a and n_0 so that:

$$y_{est}(n) - \frac{a}{n + n_0} = 0, \text{ for } n=1\dots N. \quad (\text{VII-19})$$

The above set of equation forms a linear system of N equation with two unknowns, which can be solved using a least-square method. Next, assume we have an

estimate of the parameter b , b_{est} , which contribution is subtracted from the frequency equation given in (VII-7), resulting in:

$$f_n[n] - b_{est} = \frac{a}{n + n_0} + b - b_{est}. \quad (\text{VII-20})$$

Thus, the problem becomes to fit the data $f[n]$ by finding the parameters (a, n_0) which best fit a curve of the form $a/(n+n_0)$ in a least squares sense. The set of estimated parameters has a mean-square error e_i . At this point, the problem becomes to update the parameter b , and re-estimate corresponding values for a and n_0 so that the error function expressed as a function of b is convex with a strong minimum. The location of the minimum value for the error function is obtained for b_{est} and the best estimated values of a and n_0 .

Even though we could not formally prove that the shape of the error function as a function of b is convex, we observed the same type of convex shape for the error function over 150 randomly generated hyperbolic chirps. Figure VII.4 plots the normalized errors and the mean values for a , b , and n_0 .

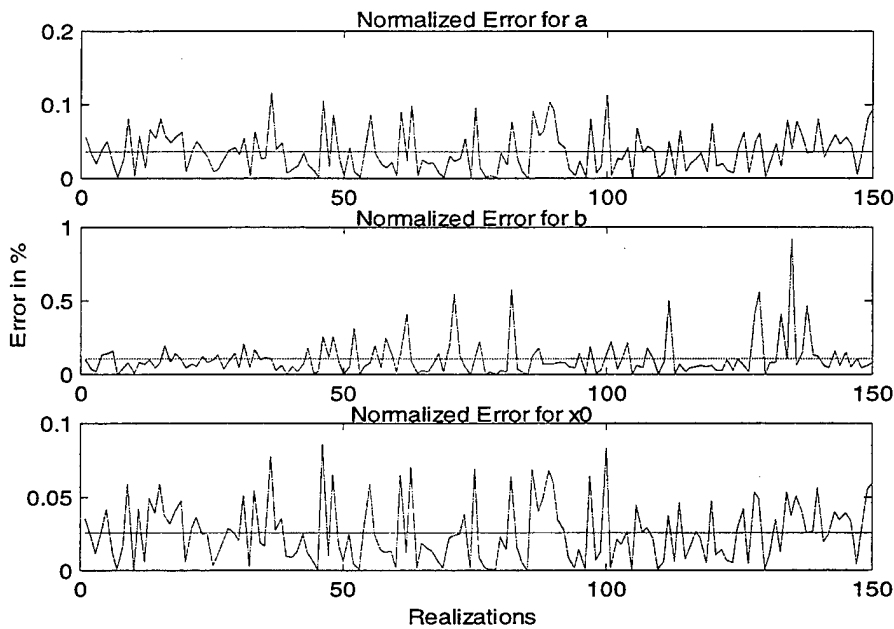


Figure VII.4: Normalized errors obtained for a , b , n_0 ; 150 randomly generated hyperbolic chirps.

The mean and standard deviation of the error is:

	Mean	Std Deviation
a	0.0361%	0.000287
b	0.1092%	0.0013
n_0	0.0262%	0.000207

Note that the mean error for b is slightly higher than that of the other two unknowns. This is to be expected, as b is restricted to the range $[0, 0.5]$. Therefore, very small error values may correspond to large normalized errors.

We adaptively estimate the value for b , by taking advantage of the convex shape of the error function. First, we restrict the search to a specific region of b . Next, we select five values of b equally spread within that range, and compute the other two parameters and the resulting mean-square error. Next, we restrict the b range to that including the minimum location by using the information provided by the mean-square errors, and repeat the process. This iterative process can be performed forever, as we have no knowledge of the minimum mean square error. In practice, we restricted the number of iterations to 10, as the values of b were restricted to small range [0,0.5] in our simulations to keep the computational load under control. Theoretically, the range of b can set as large as we want. The algorithm can converge in any area of b but it will require a larger number of iterations to preserve the same accuracy as the range of b expands, resulting in a computational load increase.

C. SIMULATION RESULTS

A few comments are in order before discussing the simulation results:

1. The scheme considered above is not as robust to noise degradations as the linear chirp scheme described in Sections V and VI. This is to be expected as a relatively clear and undistorted time-frequency image is required to extract the normalized frequency information.
2. The iterative scheme finds the set of a , b and n_0 which minimize the mean-square error. However, relatively large error values in the parameter estimates may correspond to small error in the actual hyperbolic curves. Figure VII.5 shows true and

estimated hyperbolic curves. The true parameter values are: $a=65$, $b=0.1$ and $n_0=240$, while the estimated parameter values are: $a=84$, $b=0.08$ and $n_0=294$. The normalized errors are 29%, 20% and 22% for a , b and n_0 respectively, even though the two curves are hardly different.

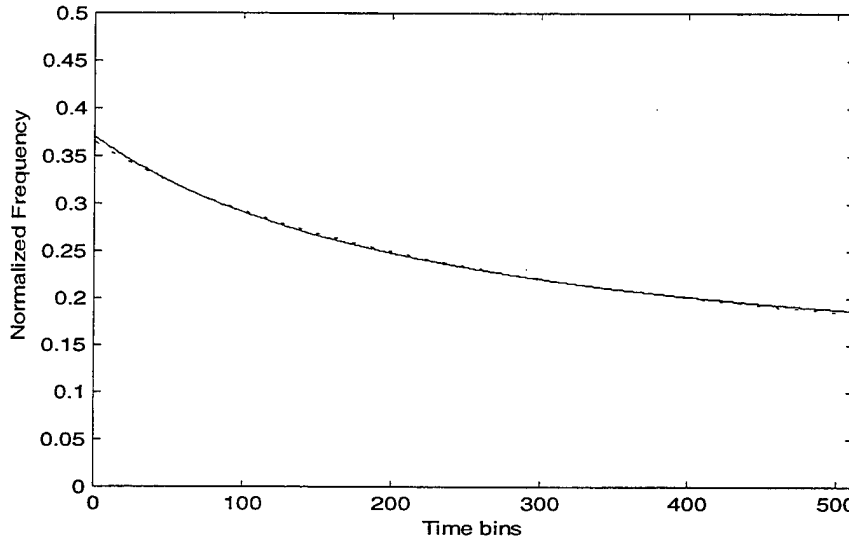


Figure VII.5: Two hyperbolic lines; Solid line: true hyperbolic curve ($a=65$, $b=0.1$ and $n_0=240$, dotted line: estimated hyperbolic curve ($a=84$, $b=0.08$ and $n_0=294$).

Hyperbolic chirps were generated by randomly selecting the parameters a , b , and n_0 in the allowed ranges mentioned earlier. Next, additive white Gaussian noise was added to generate SNR levels between 0 and 20dB, in steps of 2dB. One hundred realizations were generated for a given SNR level. Figures VII.6 to VII.8 plot the mean and the standard deviation for the normalized errors for (a, b, n_0) as a function of the SNR level, where the normalized error is defined as:

$$\text{norm error} = \frac{|\text{true value} - \text{estimated value}|}{\text{true value}} \cdot 100 \%$$

Note that the above definition may lead to large errors when the parameter true values are very close to zero, due to the denominator. Thus, we restricted our simulations to cases where b is in the range [0.025, 0.5]. The other two parameters a and n_0 are selected using the method described in section (VII-A).

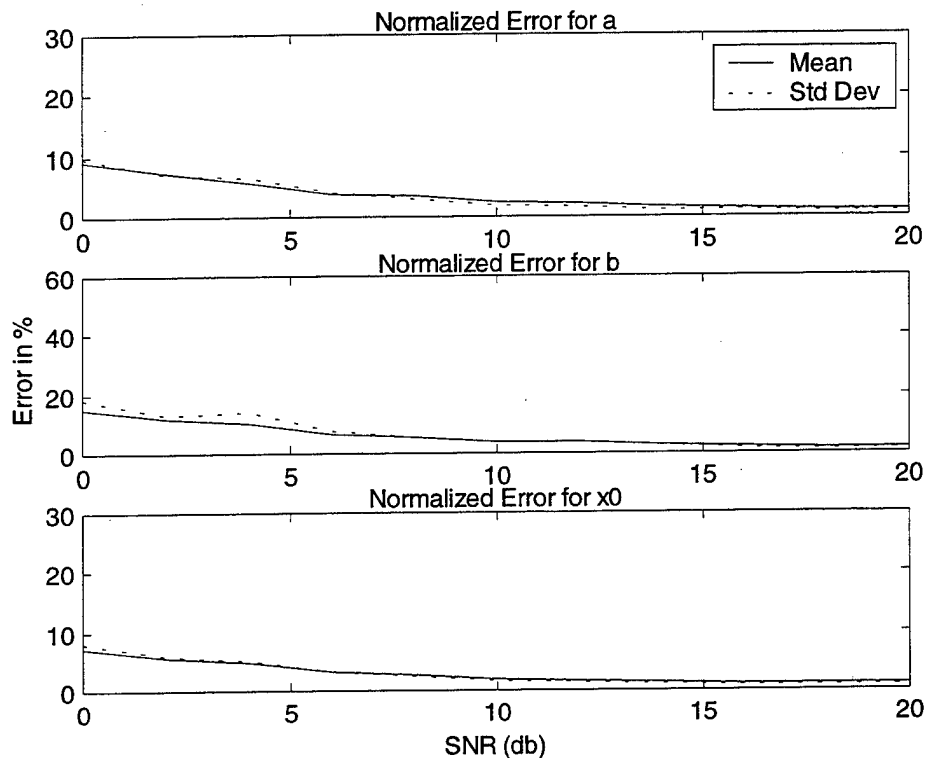


Figure VII.6: Hyperbolic chirp; normalized errors for the SPWV distribution.

Figures VII.6 to VII.8 show the normalized error mean-square and corresponding standard deviation for (a,b,n_0) obtained using the Smooth Pseudo Wigner-Ville, the Reassigned Pseudo Wigner-Ville, and the Reassigned Smoothed Pseudo Wigner-Ville distribution respectively.

Results show that the normalized errors decrease to zero as the SNR level increases. They also show that the SPWV is the scheme most robust to noise degradations out of the three considered.

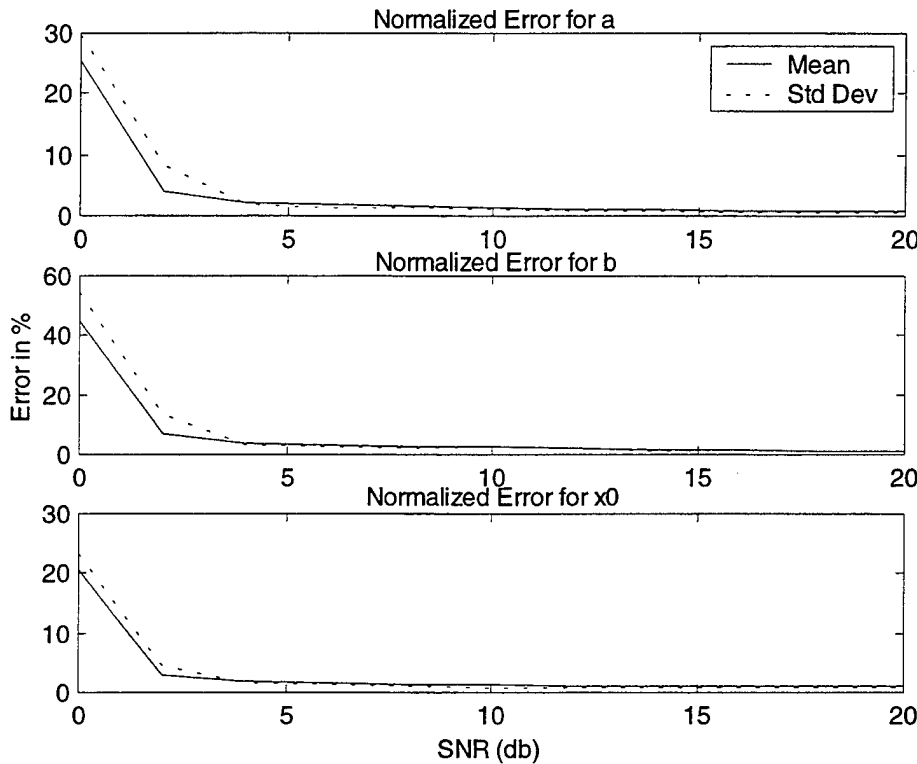


Figure VII.7: Hyperbolic chirp; normalized errors for the RPWV distribution.

Results also show that the reassigned methods perform better than the SPWV for high SNRs. This is to be expected, as they provide a more focused image by finding the center of gravity of the energy distribution for each time instance, resulting in a better image quality. However, the reassignment process worsens the image quality, as the noise level increases, resulting in the estimation process breaking down. Simulations show that

the RPWV performs slightly better than the RSPWV does, especially for SNR's in the range of 2 to 5dB.

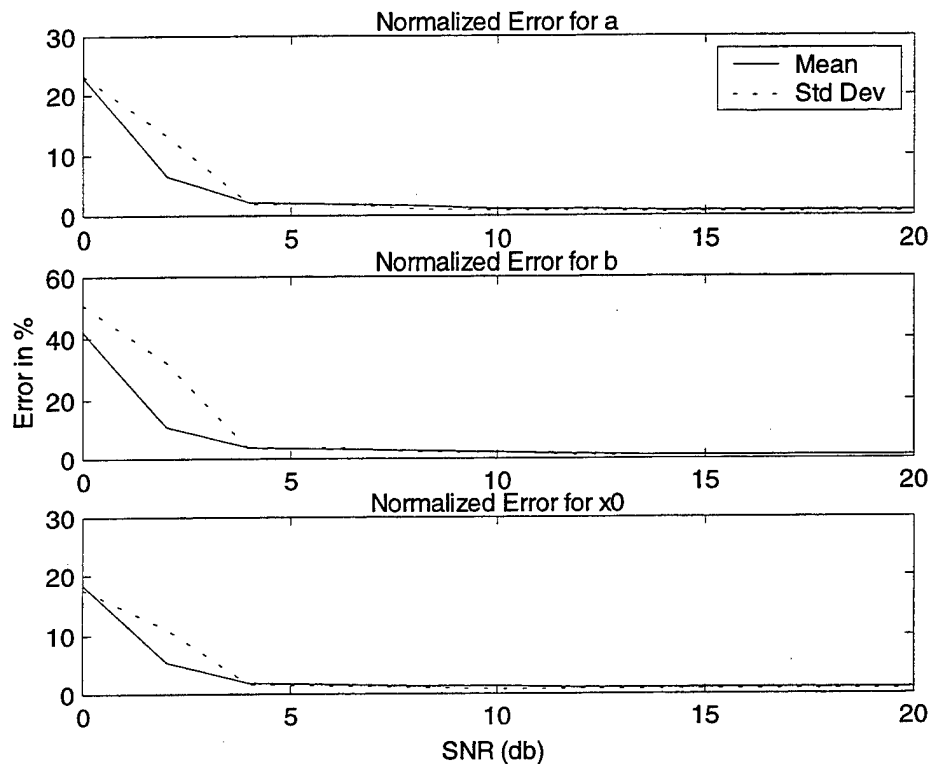


Figure VII.8: Hyperbolic chirp; normalized errors for the RSPWV distribution.

The continuous parameters A , B and t_0 in equation (VII-2) are related to the parameters of the discrete signal expression via equation (VII-6). Thus, the normalized errors estimated for the discrete values a , b and n_0 are identical to those obtained with the continuous parameters.

VIII. CONCLUSIONS

This study investigated the detection of pulse start and stop times of noisy pulsed chirp signals and the estimation of chirp modulation parameters for two specific modulation schemes; linear and hyperbolic.

The robustness of three TCF-based schemes and an envelope detection algorithm in noisy environments were compared. Results showed that none of the pulse detection schemes considered in this work to be clearly better than the others for the range of SNR levels considered, and the specific selection to be a function of the desirable characteristic (let it be P_{FA} or P_D) to be optimized.

The estimation of the modulation parameters was approached from an image processing point of view. We compared eleven different time-frequency/scale transformations and investigated their robustness to represent noisy chirps. We compared the quality of the estimated modulation parameters obtained for linear chirps when applying a Radon-based transformation to the time-frequency/scale images. Results show time-frequency transformations to lead to better focused images when dealing with noisy chirp signals, and to better estimation of the modulation parameters than wavelet-based decompositions do. Specifically, the Smoothed Pseudo Wigner-Ville distribution had the best performance in low SNR environments, while the reassignment scheme improved the performances for high SNRs. The combination of the energy distributions and the

Radon transform lead to small detection errors and almost constant performances for SNRs as low as -7dB.

Results also showed that the estimation performances increase when using multiple pulses. Simulations showed that the parameter detection SNR threshold dropped to -10dB when processing five pulses simultaneously. However, the computation time increases significantly.

Hyperbolic chirp parameters were extracted from the time-frequency image using an iterative procedure. However, this scheme requires a very good estimate of the instantaneous frequency expression as an initial estimate, thereby restricting its application to medium to high SNR levels.

This study is restricted to two specific types of modulation; linear and hyperbolic. Additional work would be needed to extend this type of approach to additional modulation types. In addition, we assumed the modulation type to be known a-priori. However, modulation identification issues need to be investigated to allow for an automated scheme to be implemented. A significant amount of work dealing with modulation identification schemes is available in the literature, each with their own advantages and drawbacks [45-47]. Further work is needed to investigate how a modulation identification scheme can be integrated with the work discussed here.

REFERENCES

- [1] B. Edde, *Radar Principles, Technology, Applications*, Prentice-Hall, Inc., 1993
- [2] S. Qian and D. Chen, *Joint Time-frequency Analysis*, Prentice-Hall, Inc. 1996
- [3] R. Barsanti, *Denoising of Ocean Acoustic Signals using Wavelet-based Techniques*, MSEE Thesis, Naval Postgraduate School, Monterey, California, December 1996
- [4] S. Mallat, *A Wavelet Tour of Signal Processing*, Academic Press, 1998
- [5] V. Wickerhauser, *Adapted Wavelet Analysis from Theory to Software*, A. K. Peters, Ltd., 1993
- [6] The Mathworks Inc., *Wavelet Toolbox*, Massachusetts, 1997
- [7] R. Coifman and M. Wickerhauser, "Entropy based algorithms for best basis selection," *IEEE Trans. on Information Theory*, Vol. 3b, No 2, March 1992
- [8] S. Mallat and Z. Zhang, "Matching pursuit with time-frequency dictionaries," *IEEE Trans. on Signal Processing*, Vol. 41 No 12, December 1993
- [9] F. Auger, P. Flandrin, P. Goncalves, O. Lemoine, *Time-frequency Toolbox Tutorial*, <http://crttsn.univ-nantes.fr/~auger/tftb.html>, 1996
- [10] L. Cohen, "Time-frequency distributions," *Proceedings of the IEEE*, Vol.77, No 7, 1989
- [11] F. Auger, P. Flandrin, P. Goncalves, O. Lemoine, *Time-frequency Toolbox, Reference Guide*, <http://crttsn.univ-nantes.fr/~auger/tftb.html>, 1996
- [12] J. Buckheit, S. Chen, D. Donoho, and J. Scargle, "Wavelab. 7.00," <http://www.wavelab/playfair.stanford.edu>, 1996
- [13] S. Deans, *The Radon Transform and Some of its Applications*, John Wiley & Sons, Inc., 1983
- [14] The Mathworks Inc., *Image Processing Toolbox*, Massachusetts, 1997
- [15] The Mathworks Inc., *Optimization Toolbox*, Massachusetts, 1997

- [16] C. Burrus, R. Gopinath, H. Guo, *A Primer Introduction to Wavelets and Wavelet Transforms*, Prentice-Hall, Inc., 1998
- [17] D. H Ballard, "Generalizing the Hough transform to detect arbitrary shapes," *Pattern recognition*, Vol. 13, No. 2, 1981
- [18] C. Therrien, *Discrete Random Signals and Statistical Signal Processing*, Prentice Hall, Inc., 1992
- [19] J. Proakis and D. Manolakis, *Digital Signal Processing Principles, Algorithms, and Applications*, Macmillan Publishing Company, 1992
- [20] A. Oppenheim, A. Willsky, S. Nawab, *Signals & Systems*, Prentice Hall, Inc., 1997
- [21] M. Skolnik, *Introduction to Radar Systems*, McGraw Hill, 1980
- [22] J. Minkoff, *Signals Noise, & Active Sensors*, John Wiley & Sons, Inc., 1992
- [23] A. Papoulis, *Probability, Random Variables, and Stochastic Processes*, McGraw Hill, 1991
- [24] U.S.Navy, Technical manual No *SE212-RB-MMO-010/SPS-40B,C,D*, Vol. 1, New York, 1985
- [25] S. Peleg and B. Porat, Linear FM signal parameter estimation from discrete-time observations," *IEEE Trans. on Aerosp. And Electronic Systems*, Vol. 27, No. 4, Jul. 1991
- [26] O. Besson, G. Giannakis, and F. Gini, "Improved estimation of hyperbolic frequency modulated chirps," *IEEE Trans. on Signal Processing*, Vol. 47, No. 5, May 1999
- [27] F. Gini and G. Giannakis, "Parameter estimation of hybrid hyperbolic FM and polynomial phase signals using the multi-lag high-order ambiguity function," Proc. 31st Asilomar Conference on Signals, Systems, and Computers, Pacific Grove, CA, Nov. 1997
- [28] S. Barbarossa and O. Lemoine, "Analysis of nonlinear FM signals by pattern recognition of their time-frequency representation," *IEEE Signal Processing Letters*, Vol. 3, No. 4, May 1996
- [29] S. Barbarossa, "Analysis of multicomponent LFM signals by a combined Wigner-Hough transform," *IEEE Trans. on Signal Processing*, Vol. 43, No. 6, June 1995

- [30] S. Barbarossa, A. Scaglione, S. Spalletta, S. Votini, "Adaptive suppression of wideband interferences in spread-spectrum communications using the Wigner-Hough transform," Proc. ICASSP '97
- [31] E. Magli, G. Olmo, and L. Lo Presti, "Pattern recognition by means of the Radon transform and the continuous wavelet transform," Signal Processing, Vol. 73, 1999
- [32] B. Gillespie and L. Atlas, "Data-driven optimization of time and frequency resolution for radar transmitter identification," Proc. SPIE Conf. on advanced signal processing: algorithms, architectures and implementations, San Diego, 1998
- [33] S. Krishnan and R. Rangayyan, "Detection of chirp and other components in the time-frequency plane using the Hough and Radon transform," IEEE Pacific Rim Conference on Communications, Computers, and Signal Processing, Aug. 1997
- [34] A. Papandreou, G. Boudreux-Bartels, and S. Kay, "Detection and estimation of generalized chirps using time-frequency representations," Proc. of the 28th Asilomar Conference on Signals, Systems, and Computers, Pacific Grove, CA, Nov. 1994
- [35] I. Moraitakis, *Feature Extraction of Intra-pulse Modulated Radar Signals using Time-frequency Analysis*, MSEE Thesis, Naval Postgraduate School, Sept. 1999
- [36] J. Wood and D. Barry, "Radon transformation of time-frequency distributions for analysis of multicomponent signals," IEEE Trans. on Signal Processing, Vol. 42, No. 11, Nov. 1994
- [37] S. Peleg and B. Porat, "Estimation and classification of signals with polynomial phase," Proc. ICASSP '89
- [38] S. Peleg and B. Porat, "Estimation and classification of polynomial-phase signals," IEEE Transactions on Information Theory, Vol. 37, No. 2, March 1991
- [39] S. Peleg and B. Porat, "The Cramer-Rao lower bounds for signals with constant amplitude and polynomial phase," IEEE Trans. on Signal Processing, Vol. 39, No. 3, March 1991
- [40] S. Peleg, B. Porat, and B. Friedlander, "The achievable accuracy in estimating the instantaneous phase and frequency of a constant amplitude signal," IEEE Trans. on Signal Processing, Vol. 41, No. 6, June 1993
- [41] *EA-165 Fundamentals of RADAR*, Prepared by: Signals, Systems and Engineering Division of the National Cryptologic School, 1998

- [42] M. Skolnik, *Introduction to RADAR Systems*, 2nd ed., McGraw-Hill Inc., 1980
- [43] R. McDonough and A. Whalen, *Detection of Signals in Noise*, pp. 76-83, 2nd ed., Academic Press Inc., 1995
- [44] A. Leon-Garcia, *Probability and Random Processes for Electrical Engineering*, pp. 246-247, Addison-Wesley publishing Company, Inc., 1994
- [45] L. Couch, II, *Modern Communication Systems Principles and Applications*, pp. 265-266, Prentice-Hall, Inc. 1995
- [46] H. Overdyk, *Detection and Classification of FH Signals using Wavelet Transforms*, MSEE Thesis, Naval Postgraduate School, Sept. 1997
- [47] N. Khalil, *Wavelet Analysis of Instantaneous Correlations with Applications to Frequency Hopped Signals*, Ph.D. Dissertation, Sept. 1997
- [48] C. Williams, *Parameter Estimation of Radar Signals*, MSEE Thesis, Naval Postgraduate School, to be completed

INITIAL DISTRIBUTION LIST

	No. Copies
1. Defense Technical Information Center 8725 John J. Kingman Rd, STE 0944 Ft. Belvoir, VA 22060-6218	2
2. Dudley Knox Library, Code 52 Naval Postgraduate School 411 Dyer Road Monterey, CA 93943-5101	2
3. Research Office, Code 09 Naval Postgraduate School 589 Dyer Road Monterey, CA 93943-5138	1
4. Chairman, Code EC Department of Electrical and Computer Engineering Naval Postgraduate School 833 Dyer Road Monterey, CA 93943-5121	1
5. Professor Ralph Hippenstiel, Code, EC/Hi Department of Electrical and Computer Engineering Naval Postgraduate School 833 Dyer Road Monterey, CA 93943-5121	2
6. Professor Monique Fargues Code, EC/Fa Department of Electrical and Computer Engineering Naval Postgraduate School 833 Dyer Road Monterey, CA 93943-5121	2
7. Professor John Powers, Code, EC/Po Department of Electrical and Computer Engineering Naval Postgraduate School 833 Dyer Road Monterey, CA 93943-5121	1